Scholars' Mine

Fall 2010

Power distribution network inductance calculation, transient current measurement and conductor surface roughness extraction

Fan Zhou

Recommended Citation

Zhou, Fan, "Power distribution network inductance calculation, transient current measurement and conductor surface roughness extraction" (2010). *Masters Theses*. 4864.
https://scholarsmine.mst.edu/masters_theses/4864

POWER DISTRIBUTION NETWORK INDUCTANCE CALCULATION,

TRANSIENT CURRENT MEASUREMENT AND CONDUCTOR SURFACE

ROUGHNESS EXTRACTION

by

FAN ZHOU

A THESIS

Presented to the Faculty of the Graduate School of the

MISSOURI UNIVERSITY OF SCIENCE AND TECHNOLOGY

In Partial Fulfillment of the Requirements for the Degree

MASTER OF SCIENCE IN ELECTRICAL ENGINEERING

2010

Approved by

Fan Jun, Advisor
Albert E. Ruehli
James L. Drewniak
Marina Koledintseva

PUBLICATION THESIS OPTION

This thesis consists of the following two articles that have been published or submitted for publication as follows:

Pages 1-32 have been accepted by EMC Symposium 2010, Fort Lauderdale, FL.

Pages 33-51 have been accepted by 2010 Asia-Pacific Symposium on EMC, Beijing.

Pages 52-69 have done for thesis writing purposes.

ABSTRACT

The first part in the thesis discussed the modeling of the mid-frequency inductance for Zpp type plane pairs in power distribution networks (PDN). It is a key step for the placement of the decoupling capacitors. This paper gives an efficient approach for the calculation of the inductance for different capacitor placements. The PEEC based formulations takes advantage of the opposite currents in the planes. This leads to compute time reductions and memory savings for both the element calculation and the matrix solve step. A formulation is used where placement of capacitors leads to only small changes in the circuit matrix. Comparisons with other models are made to validate our results.

In the second part, the application of GMI probe to measure IC switching current. IC switching current is the main noise source of many power integrity issues in printed circuit boards. Accurate measurement of the current waveforms is critical for an effective power distribution network design. In this paper, using a giant magneto-impedance (GMI) probe for this purpose is studied. A side-band detection and demodulation system is built up to measure various time-domain waveforms using an oscilloscope. It is found that the GMI probes are potentially suitable for this kind of time-domain measurements, but probe designs and measurement setups need further improvements for this application.

In the third part, the new "Sigma" rule to evaluate parameters of copper surface roughness in PCB layers is presented. This approach is based on taking SEM images of PCB cross-sections. The approach is automat zed by applying image processing tools and Matlab code to evaluate average roughness amplitude and period of roughness function. This information could be used in numerical and analytical modeling, as well as in the DERM method to separate rough conductor loss from dielectric loss.

ACKNOWLEDGMENTS

I express my sincere gratitude to Dr. Jun Fan for his constant support and guidance throughout the course of my master's degree program. I thank Prof. Ruehli, Dr. James Drewniak, Dr. Marina Koledintseva and Dr. Pommerenke for their research guidance on my work. I thank all the EMC Lab students for their help. I thank my family for their endless love and unconditional support during my study in US.

TABLE OF CONTENTS

LIST OF ILLUSTRATIONS

LIST OF TABLES

PAPER

1. EFFICIENT MID-FREQUENCY PLANE INDUCTANCE COMPUTATION
1.1

Fan Zhou, Albert E. Ruehli, Fan Jun

Electrical Engineering

Missouri University of Science and Technology, Missouri, U.S.A 65401

Email: fzm73@mst.edu, albert.ruehli@gmail.com, jfan@mst.edu

1.2 ABSTRACT

In power distribution networks (PDN), the modelling of the mid-frequency inductance for Zpp type plane pairs is very important. It is a key step for the placement of the decoupling capacitors. This research gives an efficient approach for the calculation of the inductance for different capacitor placements. The PEEC based formulations takes advantage of the opposite currents in the planes. This leads to compute time reductions and memory savings for both the element calculation and the matrix solve step. A formulation is used where placement of capacitors leads to only small changes in the circuit matrix. Comparisons with other models are made to validate our results.

Keywords

PEEC, Inductance

1.3 INTRODUCTION

Today, integrated circuits (ICs) and processors operate with internal clock frequencies of several gigahertz. Further, they demand power supply current from hundreds of milliamperes to tens of amps. The IC's demand for high speed switching current from the power delivery network (PDN) can lead to significant drops and ripples

in the supply voltage. These voltage drops are also an important issue for on chip voltage distribution networks [1].

Local, Printed Circuit Board (PCB) discrete decoupling capacitors are widely used to stabilize the power supply voltage levels by providing a low power supply impedance to meet the demand of the Integrated Circuit (IC). However, PCB inductance in the connections to decoupling capacitors limits the capacitor's ability to rapidly provide charge. Hence, the minimization of the inductance of these connections through the power plane is very important. It is well known that the decoupling capacitors are most effective for the mid-frequency ranges. At high frequencies their effectiveness is limited due to the series inductance.

Several techniques are available today to calculate via inductance [2, 3]. Full-wave electromagnetic modelling methods, transmission line methods, and analytical methods based on the cavity-model theory have been used to model the power/ground layer pair problem. However, the accurate computation of the inductances for multiple capacitor placements can be very time consuming.

In this research, an efficient approach is presented for the plane pair inductance for multiple capacitor placements. A new two-dimensional Partial Equivalent Circuit (PEEC) formulation equivalent to the 1D formulation [4] is used to calculate the partial inductance between the plane pair. The advantage of the opposite currents to reduce the inductance matrix in the system is taken in order to save time and memory use. The decoupling capacitors are modelled as shorts since at these mid-frequencies are assumed, they provide very low impedance connection. However, an inductance macromodel for the inductance of the capacitors can be included in our model. The formulation is designed so that it is easy to change the location of the capacitors by choosing the appropriate connection node. Hence, it can be used for the design of the decoupling layout and BGA power/ground pin map designs.

1.4 PLANE INDUCTANCE

1.1.1. Introduction of Partial Inductance. Self-inductance and mutual inductance are defined by loops of wire and not by the wires themselves (for thin wires). Although measurements must always be performed on closed loops – otherwise, no current flows and there is nothing to measure – calculations can be performed on pieces of closed loops. Calculation of the contributions to inductance from subsections of closed loops leads to the concept of partial inductance [7].

For thin wires, the inductance of a loop is given by Equation (1.1), which is computed on a closed contour.

$$L = \frac{\mu}{4\pi} \oint_C \oint_{C'} \frac{\overline{dl'} \cdot \overline{dl}}{|\overline{r} - \overline{r'}|}$$

(1.1)

This closed contour can be broken into any number of open contours, then

$$L = \frac{\mu}{4\pi} \sum_i \int_{C_i} \sum_j \int_{C'_j} \frac{\overline{dl'} \cdot \overline{dl}}{|\overline{r} - \overline{r'}|} = \sum_i \sum_j \left(\frac{\mu}{4\pi} \int_{C_i} \int_{C_j} \frac{\overline{dl'} \cdot \overline{dl}}{|\overline{r} - \overline{r'}|} \right)$$

(1.2)

Nothing the similarity of the bracketed portion to the definitions of inductance in Equation (1.1) and mutual inductance in Equation (1.3),

$$L = \frac{\mu}{4\pi} \oint_{C_2} \oint_{C_1} \frac{\overline{dl'} \cdot \overline{dl}}{|\overline{r} - \overline{r'}|}$$

(1.3)

The partial self-inductance is defined as

$$L = \frac{\mu}{4\pi} \int_{C_i} \int_{C'_i} \frac{\overline{dl'} \cdot \overline{dl}}{|\overline{r} - \overline{r'}|}$$

(1.4)

And the partial mutual inductance as

$$M_{ij} = \frac{\mu}{4\pi} \int_{C_i} \int_{C'_j} \frac{\overline{dl'} \cdot \overline{dl}}{|\overline{r} - \overline{r'}|}$$

(1.5)

The most important quality of the partial inductance concept is the ability to break a complicated three dimensional problem into its constituent interactions. A very simple example is given in Figure 1.1. This allows, for example, the unique attribution of voltage in the loop to constituent parts of that loop means important attributes of a design such as

the voltage drop across a return conductor, e.g., ground bounce, can be reliably computed[4].
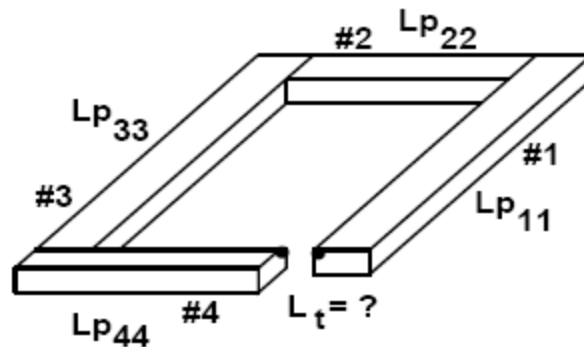
Figure 1.1. Loop and partial inductance

The equivalent circuit of the loop in Figure 1.1 is specified in terms of partial inductances   of the i-th segment and   between the i-th and j-th segments. If the loop is closed so that   , then the total loop inductance can be obtained with conventional circuit theory as

$$L=\sum_{k=1}^{4}\sum_{m=1}^{4}Lp_{km}$$

(1.6)

References contain closed form solutions for the partial inductances of conductors of various cross sections. For example, the mutual inductance between two parallel filaments of length l and separation s which are aligned is given by

$$Lp_{ij}=\frac{\mu_0}{2\pi}l(\ln(\frac{l}{s}+\sqrt{\frac{l^2}{s}+1})+\frac{s}{l}-\sqrt{\frac{s^2}{l}+1})$$

(1.7)

The self partial inductance of a wire of radius   where   is given by

$$Lp_{ii}\simeq\frac{\mu_0}{2\pi}l(\ln(\frac{2l}{r_w}-1))$$

(1.8)

Note that both expressions involve the conductor length , inside the natural logarithms so it appears that it would not be possible to define a per-unit-length value for a conductor of infinite length as is done with transmission line parameters. The formulas for conductors of rectangular cross section are quite complicated. The mutual partial inductance can often be approximated for realistically spaced conductors by resolving the conductor cross sections into filaments and summing the results as

$$Lp_{ij} \simeq \frac{1}{n_i n_j} \sum_{i=1}^{n_i} \sum_{j=1}^{n_j} Lpf_{ij}$$

(1.9)

where   is the mutual partial inductance between filaments given in Eq. (1.7). Quite often it suffices to use only one filament per conductor for these mutual partial inductance computations. The self partial inductance of a conductor of rectangular cross section is more complicated than is the mutual partial inductance. Exact results are available for special cases i.e., a thin tape.

Finally, the mutual inductance between two widely-spaced filaments can be reliably approximated in a simple fashion. Recall that the vector magnetic potential due to a current element of length at a distance from it is parallel to the filament and if   is approximated by

$$A = \frac{\mu_0}{4\pi} \frac{Il}{r}$$

(1.10)

Therefore, the mutual partial inductance between two filaments of lengths   and   which are separated by a distance   with   and have acute angle θ between them is approximated by

$$Lpf_{ij} = \frac{\int_{c_j} \vec{A} \cdot d\vec{l}_j}{I_j} \simeq \frac{\mu_0}{4\pi} \frac{l_i l_j}{r} \cos(\theta)$$

(1.11)

1.1.2. Introduction of PEEC. The Partial Equivalent Electric Circuit (PEEC) method builds up models of complex interconnect structures from simple primitive elements, such as rectangular bars, to find frequency-dependent inductance. Although many approaches are possible, the easiest is to compute the DC resistance and static partial self-inductance for each primitive element, plus the partial mutual inductance between each pair of elements. The inductances are then assembled into a complete circuit and solved with a circuit simulator. Accuracy improves with finer-grained subdivision of the original geometry. The interaction between resistance and inductance naturally leads to frequency-dependent skin effects and current crowding. Figure 1.2 shows an interconnect with two signals and a plane return path.

Since the PEEC method leads to a conventional circuit, any circuit simulation technique is applicable. For example, a full PEEC-based model of a socket can be included with driver and receiver models in a SPICE simulation. The main advantage of including the full PEEC model is that the interconnect frequency-dependent behavior is completely included. Unfortunately, this approach becomes impractical for complex PEEC models that can quickly overwhelm any circuit simulator. The next section will show the calculation time increases with the interconnects [7].

To limit the circuit size for practical circuit simulation, the size of the PEEC model must usually be reduced. Adaptive mesh can be used here. Small meshes can be used in the critical area, and in other area big cells can be used. By this methodology, the size of PEEC model can be increased.

The problem setup is the same whether a general-purpose or dedicated solver is used. All of the conductors in the problem must first be subdivided into N canonical primitive structures, such as rectangular bars, for which formulas for resistance, partial self-inductance, and partial mutual inductance are known. These small, generically shaped conductors are called branches. Many implementations are possible, but the most straightforward approach assumes that the current is uniform across the cross section of the branches. Then relatively simple DC resistance and static inductance formulas are applicable.
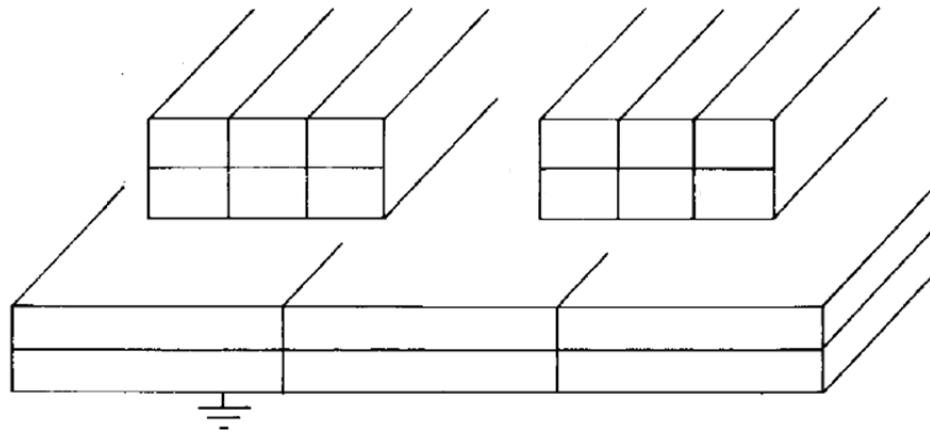
Figure 1.2. Division of conductors into segments

The resistance and partial self-inductance of each branch is computed along with the partial mutual inductance between each branch. The results can be assembled into a diagonal   resistance matrix and a dense   partial inductance matrix. The voltage drop across each branch is

$$\bar{V}_b = (\bar{\bar{R}} + j\omega\bar{\bar{L}})\bar{I}_b = \bar{\bar{Z}}_p\bar{I}_b \tag{1.12}$$

where   are the branch currents. It is assumed that the structure is subdivided in an appropriate way to enable all necessary current flow.

To complete the model of the interconnect, the branches are tied together at a number of nodes, M, where the number of nodes depends on the subdivision used. Because voltages are potential differences, one node must serve as the reference with a voltage of zero. This node, called the datum node, is not included in the problem setup – it is assumed. The same situation occurs in general-purpose circuit simulators such as SPICE, where the datum node is labeled as "0" and forms the ground reference.

At this point, the interconnect has been break into its component parts and modeled with a circuit consisting of resistances and partial self- and mutual inductances. The circuit must be solved with either a general-purpose or dedicated simulator.

A dedicated solver for the PEEC method can be constructed by satisfying Kirchhoff's voltage and current laws for the branch voltages and currents. The goal is to

eliminate the branch voltages and currents in favor of node voltages and currents. Then the nodes internal to the circuit can be eliminated to obtain a simplified model relating just the external nodes, or ports. The model is used by connecting the ports to other system components, such as drivers and receivers.

The branch voltages are related to the node voltages by differences: the difference of the two node voltages at the ends of a branch is the branch voltage. This relationship for the entire problem can be stated as:

$$\bar{V}_b = \bar{\bar{A}}\bar{V}_n \qquad\qquad (1.13)$$

where   , called the incidence matrix, stores all of the connection information in an

matrix. It can be constructed by setting   and   when the current flows from node i to node j through branch b.

The total current into the nodes is given by:

$$\bar{I}_n = \bar{\bar{A}}^T \bar{I}_b \qquad\qquad (1.14)$$

where   are the branch currents driven by the branch voltagesm and   are currents driven into the nodes by external sources.

1.1.3. Plane Subdivision. Our new reduced PEEC based model can be applied to complex plane structures with multiple shorts at the locations of the decoupling capacitors and with multiple current excitations. In this research, the dc resistance is not considered. However, this is not a fundamental limitation of the technique. The conductors are assumed to have zero thickness and that the skin-effect is not included. This is very acceptable for the type of inductance estimation which performed in this research since the skin-effect represents a small fraction of the inductance with the exception of very close spaced planes. The formulation is kept as simple as possible so that the compute time is minimal. This way, the computation of different decoupling capacitors arrangement can be computed without excessive compute time.

For the plane pairs, the planes are subdivided into commensurate cells for which the partial inductances are evaluated.

Figure 1.3 shows the subdivision of the planes. Importantly, the same divisions must be used for both planes. The width of the cells on the edge is just half of the cells in the middle such that a uniform edge-connected node meshes results as the case for the

conventional PEEC meshing. This allows the joining of different plane sections to be connected together in a systematic way.
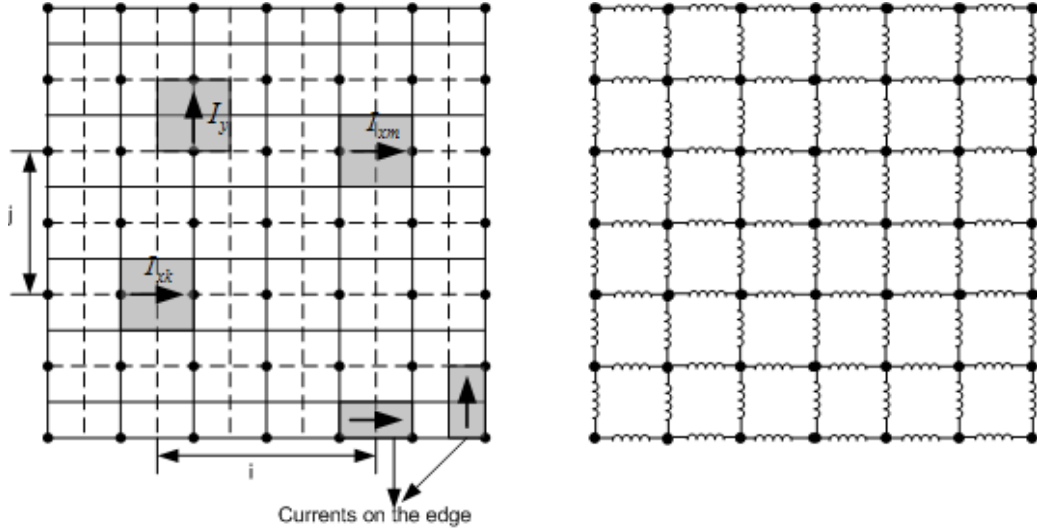
Figure 1.3. Subdivision of planes

The partial inductances between the cells can be computed analytically, which is shown in Figure 1.4. A closed form expression for zero thickness planes give as Eq. (1.15) [5] is used.

$$Lp_{ij} = \frac{\mu}{4\pi} \frac{1}{W_i W_j} \sum_{k=1}^{4}\sum_{m=1}^{4} (-1)^{m+k} [\frac{b_m^2 - C^2}{2} a_k \log(a_k + \rho) + \frac{a_k^2 - C^2}{2} b_m \log(b_m + \rho)$$

$$- \frac{1}{6}(b_m^2 - 2C^2 + a_k^2)\rho - b_m C a_k \tan^{-1}\frac{a_k b_m}{\rho C}]$$

(1.15)

where

$$\rho = \sqrt{a_k^2 + b_m^2 + C^2}$$

and

$$a_1 = a_{ij} - \frac{f_a}{2} - \frac{s_a}{2}, \quad a_2 = a_{ij} + \frac{f_a}{2} - \frac{s_a}{2},$$

$$a_3 = a_{ij} + \frac{f_a}{2} + \frac{s_a}{2}, \quad a_4 = a_{ij} - \frac{f_a}{2} + \frac{s_a}{2}$$

$$b_1 = b_{ij} - \frac{f_b}{2} - \frac{s_b}{2} \ , \ b_2 = b_{ij} + \frac{f_b}{2} - \frac{s_b}{2}$$

$$b_3 = b_{ij} + \frac{f_b}{2} + \frac{s_b}{2} \ , \ b_4 = b_{ij} - \frac{f_b}{2} + \frac{s_b}{2}$$
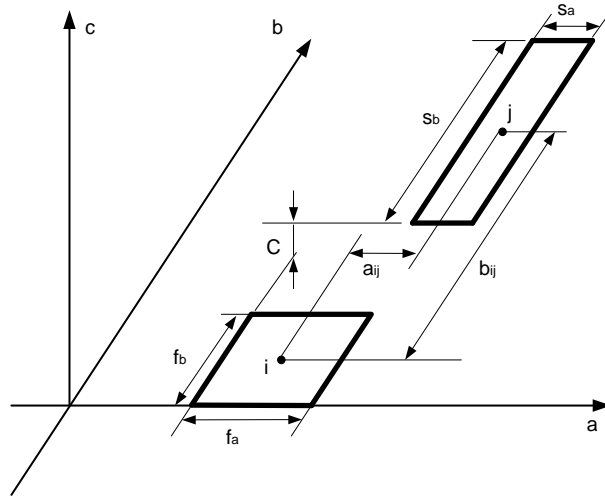
Figure 1.4. Two zero thickness planes

1.1.4. Sparse Inductance Model. As the case for the Zpp model, there are two planes with opposing currents. Hence, the units of cell pairs consisting of two cells located in the same x,y position are considered as one section. A key advantage is the fact that the inductive coupling between the distant cells drops off fast due to the cancelling dipole effect of the opposing currents on the cell pairs. This leads to a sparse matrix in the coupling in the inductive coupling matrices. This has been shown to be the case for transmission lines [4]. As a result, the positive definiteness of the matrix is much easier to guarantee.

The mutual coupled voltage between the cells is given in from Figure 1.5 with the equivalent circuit shown in the Figure 1.6 as Eq. (1.16)

$$V_a - V_b = (Lp_{km'} - Lp_{k'm} + Lp_{km} - Lp_{k'm'})sI_m \tag{1.16}$$

Since the cells are in the same plane, the symmetry to simplify the equation to Eq. (1.17) can be applied. This saves a factor two in the number of partial inductance evaluations.

$$Ls_{km} = \frac{V_a - V_b}{sI_m} = 2(Lp_{km} - Lp_{km'}) \tag{1.17}$$
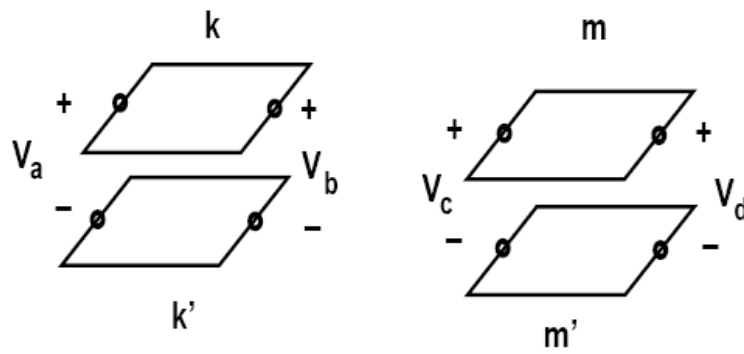
Figure 1.5. Cell pair to cell pair coupling
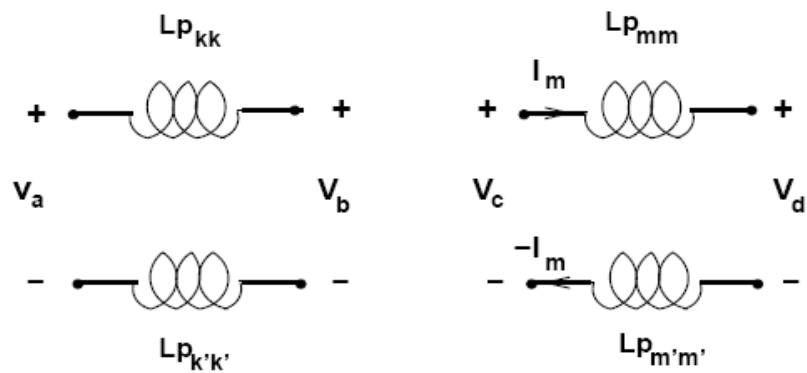
Figure 1.6. Equivalent circuit for cell pair coupling

The magnetic vector potential due to a current element of length at a distance from it is parallel to the filament and if is approximated by:

$$A = \frac{\mu_0}{4\pi} \frac{Il}{r}$$ (1.18)

Therefore, the partial mutual inductance between two filaments of lengths and which are separated by a distance with and have acute angle θ between them is approximated by:

$$Lp_{ij} = \frac{\int_{c_j} \vec{A} \cdot d\vec{l}_j}{I_i} = \frac{\mu_0}{4\pi} \frac{l_i l_j}{r} \cos(\theta)$$ (1.19)

Next, the section-to-section coupling in Eq. (1.17) decreases rapidly with the section-to-section distance for the plane pair is studied. The mutual inductance between two different sections and is calculated as an example as shown in Figure 1.3.

According to Eq. (1.19):

$$Lp_{km} = 0.1 \frac{\Delta x \Delta y}{\sqrt{(i\Delta x)^2 + (j\Delta y)^2}}$$ (1.20)

$$Lp_{km'} = 0.1 \frac{\Delta x \Delta y}{\sqrt{(i\Delta x)^2 + (j\Delta y)^2} \sqrt{1+q^2}}$$ (1.21)

Respectively, with

$$q = \frac{h}{\sqrt{(i\Delta x)^2 + (j\Delta y)^2}}$$ (1.22)

is the plane to plane spacing and is the section length. The square root can be expanded in a Taylor series as

$$(1+q^2)^{-\frac{1}{2}} = 1 - \frac{q^2}{2} + \frac{q^4}{8} - \cdots$$

for . The mutual inductance between sections becomes

$$Ls_{km} = 0.1\Delta x \Delta y q^2 / \sqrt{(i\Delta x)^2 + (j\Delta y)^2}$$ (1.23)

where and again . The second condition most likely leads to

.

Here, the cell size as 1 mm x 1 mm and the spacing between the two planes as 0.2 mm is considered as our example. The distance between two sections is defined as

. Figure 1.7 shows the comparison between the decay of ,

and   normalized to self-inductance with different distances when the section k and section m are both in the middle of the plane.

From Figure 1.8, it is evident that when the distance between two sections is much larger than the space between two planes since   and   are very close. The mutual inductance between two sections   are very small and decays more rapidly than   and   with distance increases. At the relatively short distance of 50 mm, the coupling is clearly extremely small. Hence, a very sparse matrix results for large plane problems.

Table 1.1 shows a comparison of approximation results with different distances. From this analysis, it is shown that the error of the approximate results decreases quickly as distance increases. For the 0.2 mm space and 1 mm x 1 mm cell case, the error in the approximation decreases rapidly and the relative error normalizes to the mutual inductance is given by   is less than 3% if the distance is larger than 5 mm and smaller than 50 mm. If normalized to the self inductance, the error   is less than 5.414e-6.
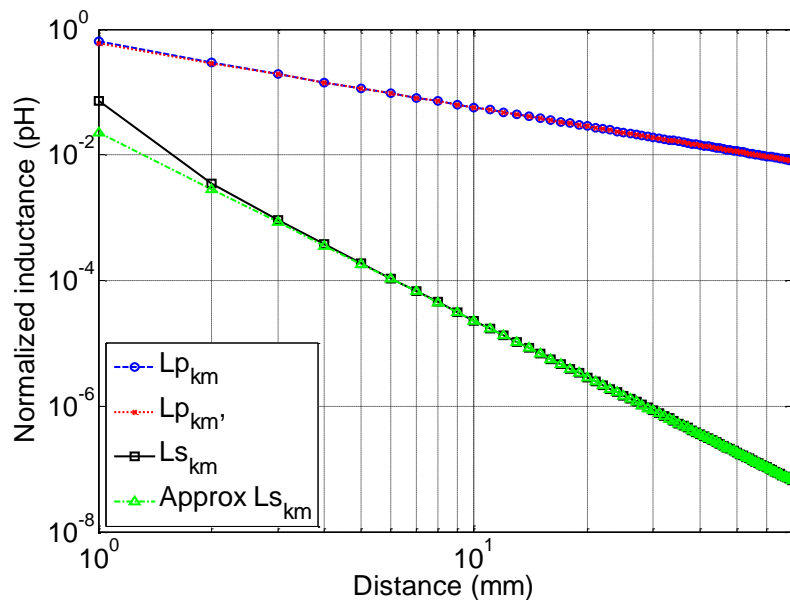
Figure 1.7. The decay of mutual inductance
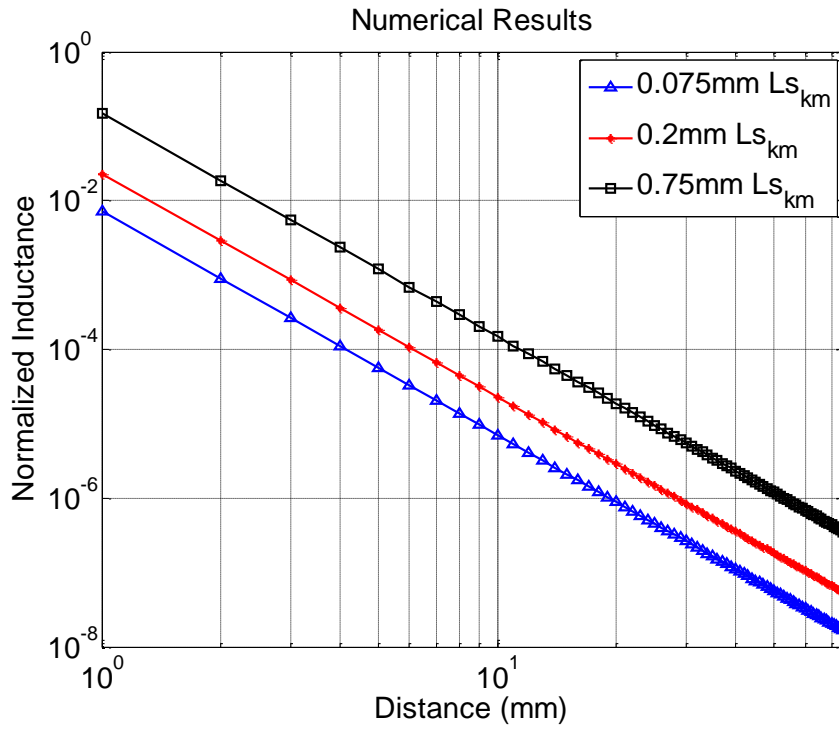
Figure 1.8. Normalized inductance as function of planes distance h

Table 1.1. COMPARISON OF APPROXIMATION RESULTS

Distance	Ls_{km1} (pH)	Ls_{km} Approx (pH)	Error (%)
1 mm	12.5950	4.0000	68.2414
2 mm	0.6063	0.5000	17.5326
3 mm	0.1609	0.1481	7.9021
5 mm	0.0329	0.0320	2.8672
8 mm	0.0079	0.0078	1.1230
10 mm	4.0290e-3	4.0000e-3	7.1920e-1
15 mm	1.1890e-3	1.1852e-3	3.1985e-1
50mm	3.2004e-5	3.2000e-5	1.2583e-2

Hence, the decay in the mutual cell-pair to cell-pair coupling decays fast. For example, when the distance is larger than 10 mm, the mutual section inductance is smaller than 0.004 pH.

According to Eq. (1.23), the normalized inductance:

$$L_n = \frac{Ls_{km}}{Ls_{kk}} = \frac{0.1\Delta x \Delta y h^2}{r^3 Ls_{kk}} \tag{1.24}$$

is the self inductance of k-th section. It relates to the section length, width and the space of plane pair is 0.075mm. Figure 1.8 shows the normalized inductance when the space of the plane pair is 0.075 mm, 0.2 mm and 0.75 mm. The mesh size is 1mm x 1mm. Of course, the inductive coupling or the normalized inductance increases for an increase in the plane distance.

1.1.5. Model for Planes. The above analysis can be directly applied to this example. The matrix is assembled by stamping in the appropriate contribution circuit element by element in a conventional Modified Nodal Analysis (MNA) way to form the circuit matrix. MNA matrix stamps can be used to set up the circuit matrix.

Table 1.2 is a matrix stamp for two coupled partial inductances. For the shorts, the voltage source stamp is used as shown in Table 1.3 as is conventionally done. RHS is the right-hand side of KVL and KCL equations, m1 and m2 are the m1-th and m2-th node. Aux1 means the current in the Aux1's branch and Aux2 means the current in the Aux2's branch.

Table 1.2. MNA MATRIX STAMP FOR TWO COUPLED PARTIAL INDUCTANCES

Row\Col	V_1	V_2	I_1	I_2	RHS
m1			1	-1	
m2			-1	1	
Aux$_1$	1	-1	$-sLp_{11}$	$-sLp_{12}$	
Aux$_2$	-1	1	$-sLp_{21}$	$-sLp_{22}$	

Table 1.3. MNA MATRIX STAMP FOR VOLTAGE SOURCE

Row\Col	V_1	V_2	I_s	RHS
m1			-1	
m2			1	
Aux$_1$	1	-1		Vs

Figure 1.9 represents the smallest possible illustrative example for the two plane representations. Each of the connection includes a partial inductance. As shown in Figure 1.5, node N1 is shorted and a current is injected into node N4. If looked at node N4, the self inductance is given by   . The circuit equations for our small example are given in Eq. (1.25). By solving this system, all the voltages at each node and the currents in each branch can be calculated. Then all other desired inductances like L_{42} and L_{43} can be calculated.
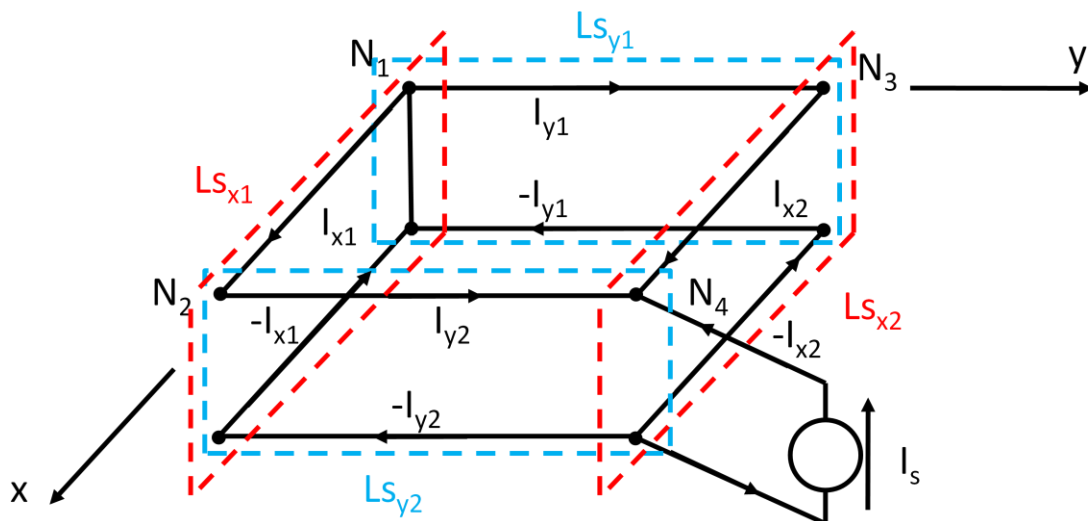

Figure 1.9. Smallest possible example problem for two planes

Importantly, the structure of the matrix is the same for a larger, more realistic example with N > 4. The current can be injected at any Node(s) to compute the inductance. Also, the appropriate shorts can be placed at nodes where the capacitances are placed. Note that the shorts and excitations can be placed at the last row and column of the matrix such that the rest of the matrix is not touched by different placements. Again, the last columns and rows of the symmetric matrix are used for the voltage source (shorts) stamp in Table 1.3. It is obvious that several capacitors can be added by adding more rows and columns without re-computing the time-expensive remainder of the matrix.

1.1.6. Numerical Experiments for Uniform Mesh. The size of our experiments is mostly limited by the 16 GByte memories available on the PC used. It is evident from the experimental results given below that compute time it is not a limitation. An example is tested where the plane pair size is 50mm x 50mm in size and the space of the plane pair is 0.2 mm. The short is located at (x=25.25mm, y=12.25mm) and the port is at (x=25.25mm, y=37.75mm). The geometry is shown in Figure 1.10. Two different mesh sizes are used for the first examples where the computation time are compared. For the first example 45 cells are used in both the x and y directions. To validate with other solutions, PowerPEEC program [8] and the Hybrid method approach are ised [3].

A comparison of the compute time for the different approaches is given in Table 1.4. Eq. (1.15) and Eq. (1.17) are used to compute the exact partial and pair mutual inductance between the sections for a distance smaller than 10 mm and spacing between the two planes of 0.2 mm. For the distance larger than 10 mm and smaller than 15 mm, the approximate Eq. (1.23) is used. Further, for a distance larger than 15 mm, the partial mutual inductances are set to 0 due to the very small coupling.

Table 1.4 shows that the computed inductances match the PowerPEEC and Hybrid method very well and the results for the approximations are close. Importantly, the compute time is reduced by more than 8 times by the approximations. All our results are obtained with an experimental Matlab code. The compute time for PowerPEEC and the Hybrid solution are given here, due to the different implementation and computers used. For example PowerPEEC is implemented in C++ and it runs on Linux. However, this clearly should not impact the results obtained.

$$
\begin{bmatrix}
0 & 0 & 0 & 0 & 1 & 0 & 1 & 0 & 1 \\
0 & 0 & 0 & 0 & -1 & 0 & 0 & 1 & 0 \\
0 & 0 & 0 & 0 & 0 & 1 & -1 & 0 & 0 \\
0 & 0 & 0 & 0 & 0 & -1 & 0 & -1 & 0 \\
1 & -1 & 0 & 0 & -Lx_{11} & -Lx_{12} & 0 & 0 & 0 \\
0 & 0 & 1 & -1 & -Lx_{12} & -Lx_{22} & 0 & 0 & 0 \\
1 & 0 & -1 & 0 & 0 & 0 & -Ly_{11} & -Ly_{12} & 0 \\
0 & 1 & 0 & -1 & 0 & 0 & -Ly_{12} & -Ly_{22} & 0 \\
1 & 0 & 0 & 0 & 0 & 0 & 0 & 0 & 0
\end{bmatrix}
\begin{bmatrix}
V_{N1} \\ V_{N2} \\ V_{N3} \\ V_{N4} \\ sI_{x1} \\ sI_{x2} \\ sI_{y1} \\ sI_{y2} \\ sI_{sh}
\end{bmatrix}
=
\begin{bmatrix}
0 \\ 0 \\ 0 \\ I_s \\ 0 \\ 0 \\ 0 \\ 0 \\ 0
\end{bmatrix}
\tag{1.25}
$$

50mm x 50mm
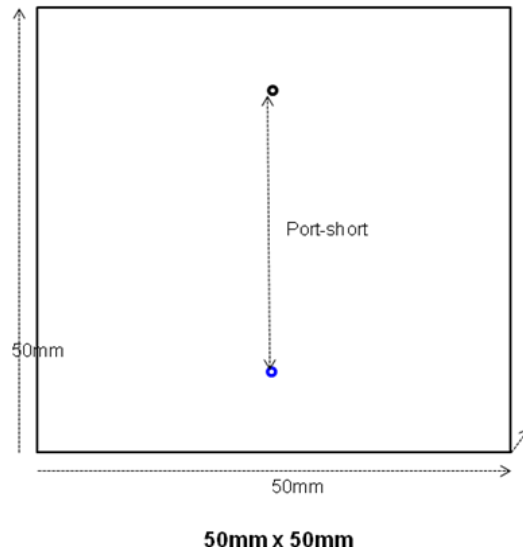
Figure 1.10. Single short test geometry

The calculation results and time are shown in the Table 1.4.

Table 1.4. CALCULATION RESULT

	Unknowns	Inductance (pH)	Time (s)
Without Approx	5986	366.5	401.9
With Approx	5986	366.3	52.9
PowerPEEC[8]	------	377.7	------
Hybrid	------	367.0	------

Our MNA matrix is composed of several distinct parts. Figure 1.11 shows the small example in Figure 1.9. The dashed curve corresponds to the plane inductance model which remains fixed even if the ports and shorts (capacitors) are changed.

Figure 1.12 gives the compute time for the matrix which shows that for small problems, most of the compute time is spent to generate the MNA matrix. The blue curve is the matrix compute time while the green curve is the total time. However, it is also evident that for larger problems the matrix solves time (red curve) is eventually going to dominate the compute time for large problems. However, the symmetric matrix with a very predictable form is ideally suited for a special purpose sparse matrix solution. The matrix structure is planed to exploit even further for the case where the configuration of the decoupling capacitors (shorts) is changed multiple times for the improvement of the capacitor layout.

Importantly, the port and shorts locations can be changed without re-computing the computationally more expensive inductance computation parts. To validate this, a test geometry with multi-shorts is used. As a last experiment, an example is given where the shorts are changed in the layout. As has been pointed out above, this results in relatively minor changes in the solution. A example in Figure 1.10 with one port and one shorted via is studied. As a second example, the shorts layout are changed to the case shown in Figure 1.13, which has five shorts located at (15, 40), (20, 40), (25, 40), (30, 40), (35, 40). For simplicity, only one observation port again at (25, 10) is calculated. The inductance

result obtained for this case is 305.75 pH while the computation with PowerPEEC resulted 306.78 pH. The difference between the two results is only 0.34% which is an excellent match. Table 1.5 confirms that the difference in compute time due to the increased number of shorts is minimal. As is evident also, the number of unknowns due to the additional shorts increased only by four.

$$
\begin{bmatrix}
0 & 0 & 0 & 0 & 1 & 0 & 1 & 0 & 1 \\
0 & 0 & 0 & 0 & -1 & 0 & 0 & 1 & 0 \\
0 & 0 & 0 & 0 & 0 & 1 & -1 & 0 & 0 \\
0 & 0 & 0 & 0 & 0 & -1 & 0 & -1 & 0 \\
1 & -1 & 0 & 0 & -Lx_{11} & -Lx_{12} & 0 & 0 & 0 \\
0 & 0 & 1 & -1 & -Lx_{12} & -Lx_{22} & 0 & 0 & 0 \\
1 & 0 & -1 & 0 & 0 & 0 & -Ly_{11} & -Ly_{12} & 0 \\
0 & 1 & 0 & -1 & 0 & 0 & -Ly_{12} & -Ly_{22} & 0 \\
1 & 0 & 0 & 0 & 0 & 0 & 0 & 0 & 0
\end{bmatrix}
$$

Figure 1.11. MNA matrix
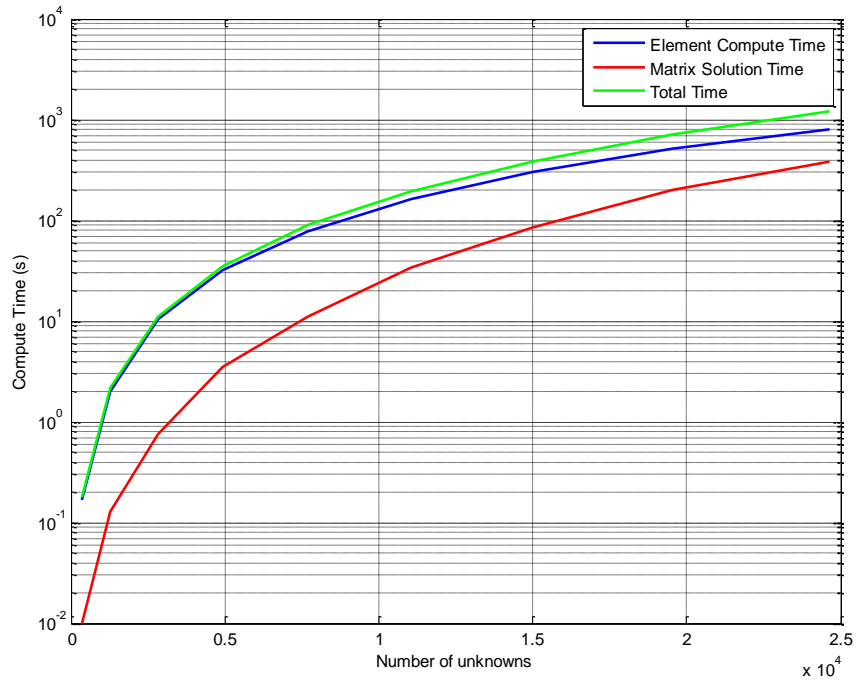
Figure 1.12. Calculation time
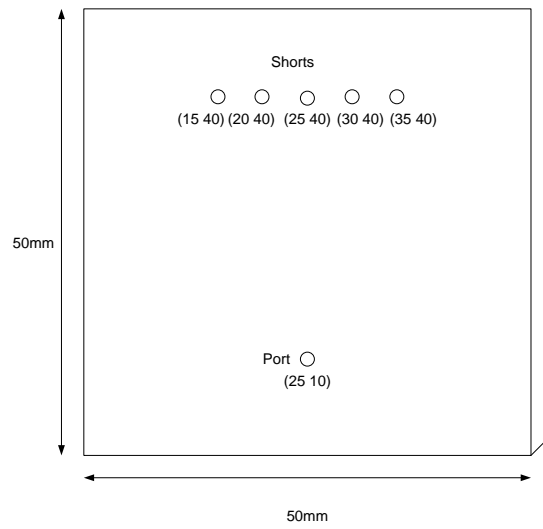
Figure 1.13. Multi-shorts test geometry

Table 1.5. SINGLE SHORT AND MULTI-SHORTS

Shorts Numbers	1	5
Unknowns	11042	11046
Time (s)	195.3	198.1

Again in all the experiments PC computer with 16 GByte of RAM and 2 GHz CPU was used.

1.1.7. Adaptive Mesh. To limit the circuit size for practical circuit simulation, the size of the PEEC model must usually be reduced. A large reduction in cells may be possible by using a non-uniform mesh.

The MNA matrix is composed of KVL and KCL equations as shown in Figure 1.14. The Mesh for x direction is shown in Figure 1.15.

$$
\begin{bmatrix}
0 & 0 & 0 & 0 & 1 & 0 & 1 & 0 & 1 \\
0 & 0 & 0 & 0 & -1 & 0 & 0 & 1 & 0 \\
0 & 0 & 0 & 0 & 0 & 1 & -1 & 0 & 0 \\
0 & 0 & 0 & 0 & 0 & -1 & 0 & -1 & 0 \\
1 & -1 & 0 & 0 & -Ls_{x11} & -Ls_{x12} & 0 & 0 & 0 \\
0 & 0 & 1 & -1 & -Ls_{x12} & -Ls_{x22} & 0 & 0 & 0 \\
1 & 0 & -1 & 0 & 0 & 0 & -Ls_{y11} & -Ls_{y12} & 0 \\
0 & 1 & 0 & -1 & 0 & 0 & -Ls_{y12} & -Ls_{y22} & 0 \\
1 & 0 & 0 & 0 & 0 & 0 & 0 & 0 & 0
\end{bmatrix}
\begin{matrix} \text{KCL} \\ \\ \\ \\ \text{KVL} \\ \\ \\ \\ \end{matrix}
$$

Figure 1.14. MNA matrix separation

The difficulty is to write the MNA matrix in the transition area from big cells to small cells. Here some assumptions are used. When considering the KVL part in MNA matrix, all the cells are calculated including the mutual inductance information between any two different cells.

When considering the KCL part in MNA matrix, the current distribution is uniform in each different sectoin is assumed. There are three possible cases as Node A, Node B and Node C in Figure 1.15.

For Node A, the KCL equation is:

$$-0.75I_1 + I_4 = 0 \tag{1.26}$$

For Node B, the KCL equation is:

$$-0.25I_1 - 0.25I_2 + I_5 = 0 \tag{1.27}$$

For Node C, the KCL equation is:

$$-0.5I_2 + I_6 = 0 \tag{1.28}$$

Figure 1.15. Adaptive mesh in x direction

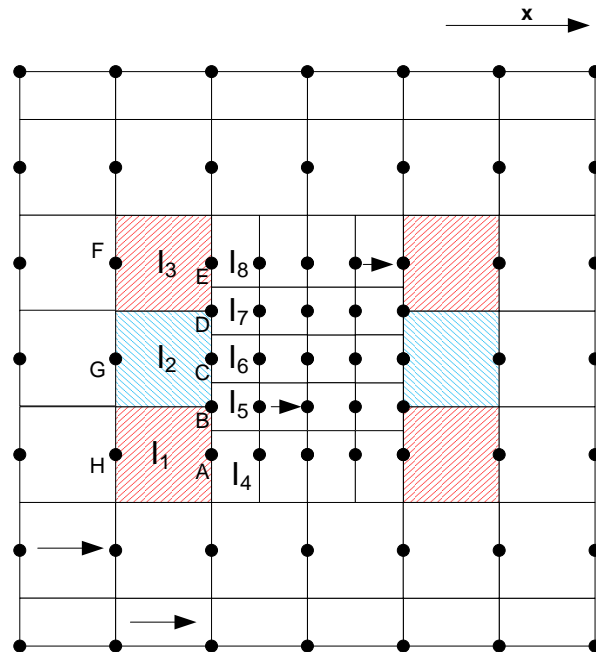The same method can be used in y-direction. Then a new MNA matrix can be got. By solving the matrix equation, the inductance can be calculated.

Because the current distribution will focus to the port and shorts, the small mesh size can be used in this region. For the region which is far away from port and shorts, the big mesh size can be used. By using this method, the calculation accuracy changes a little, but the unknowns and calculation time decreased a lot.

This method also has one disadvantage. The MNA matrix has to be re-generated each time if any change about port or shorts has been made.

A combination of uniform mesh and adaptive mesh can be used to calculation real structure. First, uniform mesh is used to find out which position is best to put de-coupling capacitors. Then, adaptive mesh is used to calculation high accuracy result.

1.1.8. Numerical Experiments for Adaptive Mesh. The same testing computer is used to test the adaptive mesh. The plane pair is 10 mm   10 mm, the prot is at (2.5, 2.5) and the short is at (7.5, 7.5). The space between two planes is 0.8 mm. The size of our experiments is mostly limited by the 16 GByte memories available on the PC used.

First, the calculation result between uniform mesh and adaptive mesh is compared. For the uniform mesh, 33 cells are used in both x and y direction. For the adaptive mesh, the small mesh cell is the same as the mesh cell in uniform mesh. The big mesh cell is twice as the small ones. The different adaptive areas are also tested. The mesh is shown in Figure 1.16.

The calculation result is shown in the Table 1.6 . The unknowns of adaptive mesh are close to one third of unknowns for uniform mesh, and the calculation time is only one seventh of the uniform mesh. But the difference between two calculation results is 0.32%. By using adaptive mesh, more mesh cells with less calculation time can be calculated and the accuracy keeps almost the same.

Second, the convergence of adaptive mesh has been checked. The calculation results will convergence with the adaptive area increase. From Figure 1.17, it shows that as the adaptive area increase, the calculation results convergence. Figure 1.18, Figure 1.19 and Figure 1.20 are the voltage distribution and current distribution. From these distributions, it is easy to see that the current focus at the port and short. When the cell is far away from port and shorts, the current is very small. They can be ignored.

Figure 1.21 gives the compute time for different unknowns. From Figure 1.21 it shows that, the calculation time increase faster than unknowns. The unknowns increase 10 times, the calculation time increase more than 100 times.
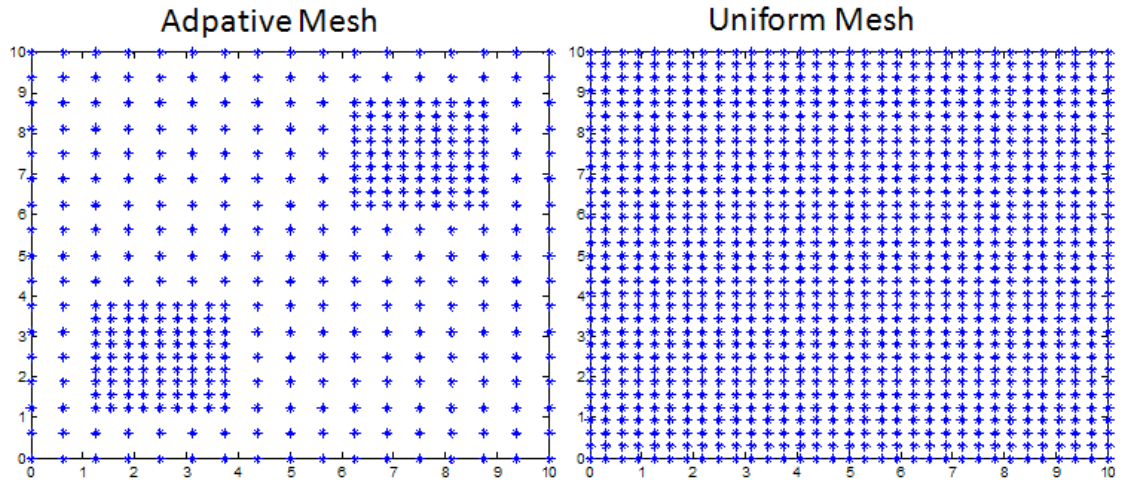
Figure 1.16. Comparison between uniform mesh and adaptive mesh

Table 1.6. ADAPTIVE MESH AND UNIFORM MESH

	Adaptive Mesh	Uniform Mesh	PowerPEEC
Unknowns	922	3202	------
Inductance (pH)	1019.2	1022.6	1023.4
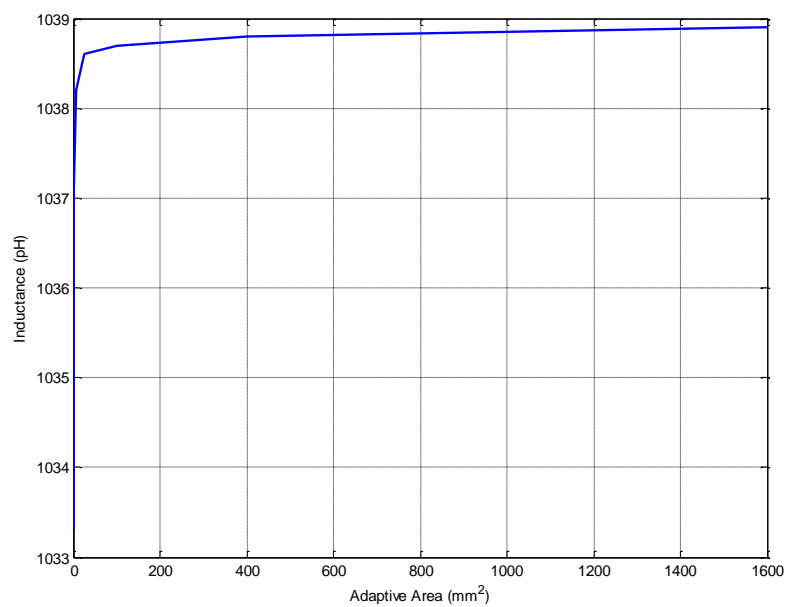
Figure 1.17. Convergence
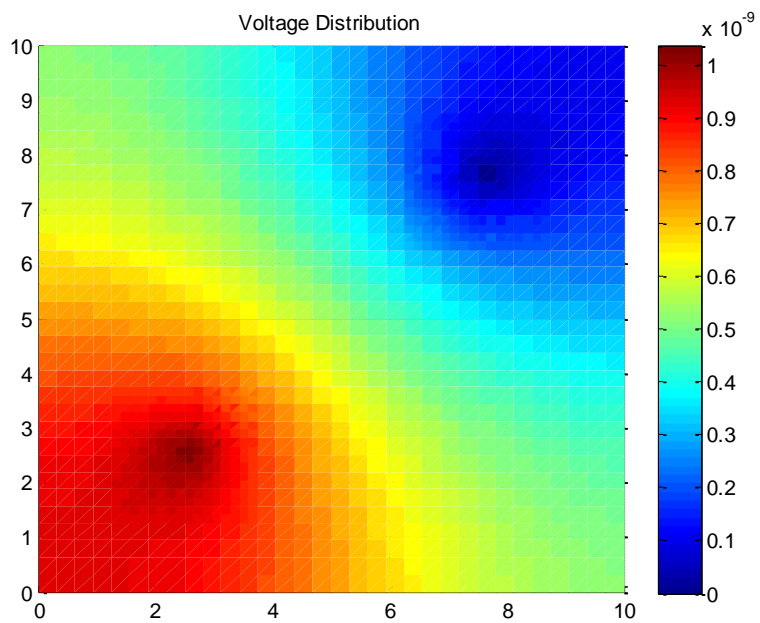
Figure 1.18. Voltage distribution
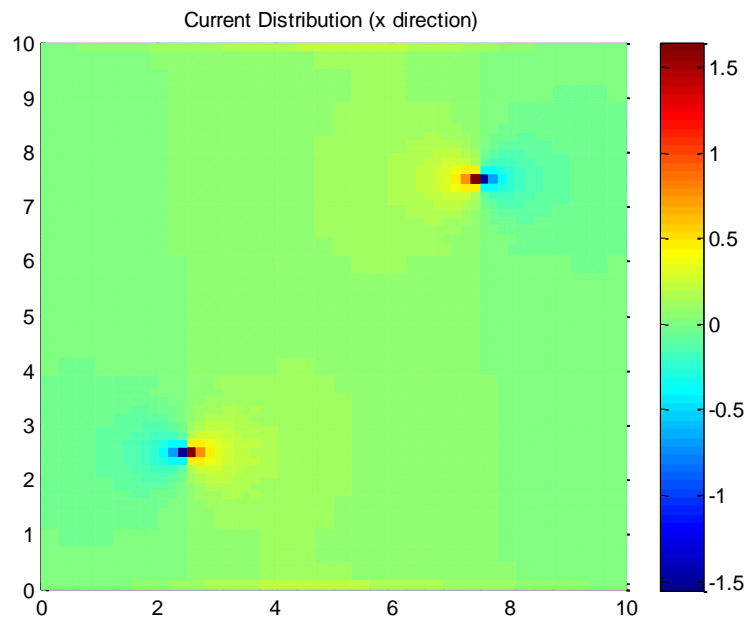
Figure 1.19. Current distribution in x direction
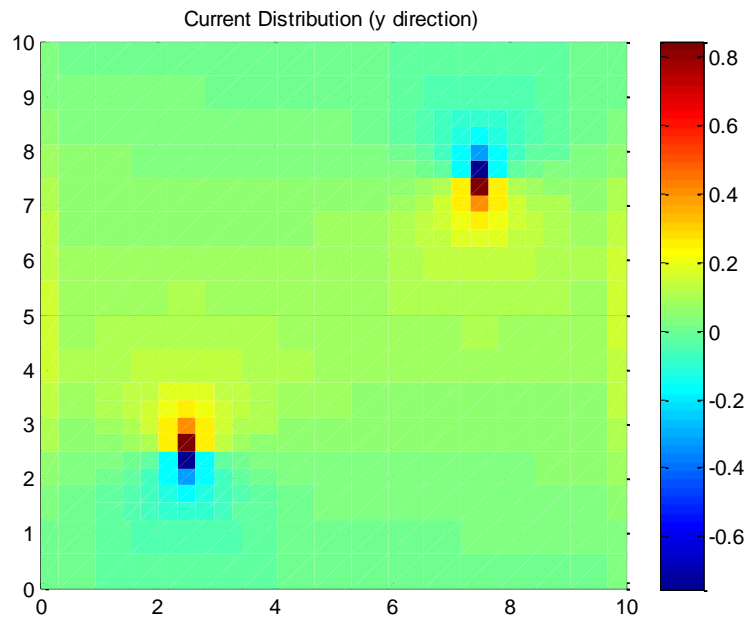
Figure 1.20. Current distribution in y direction
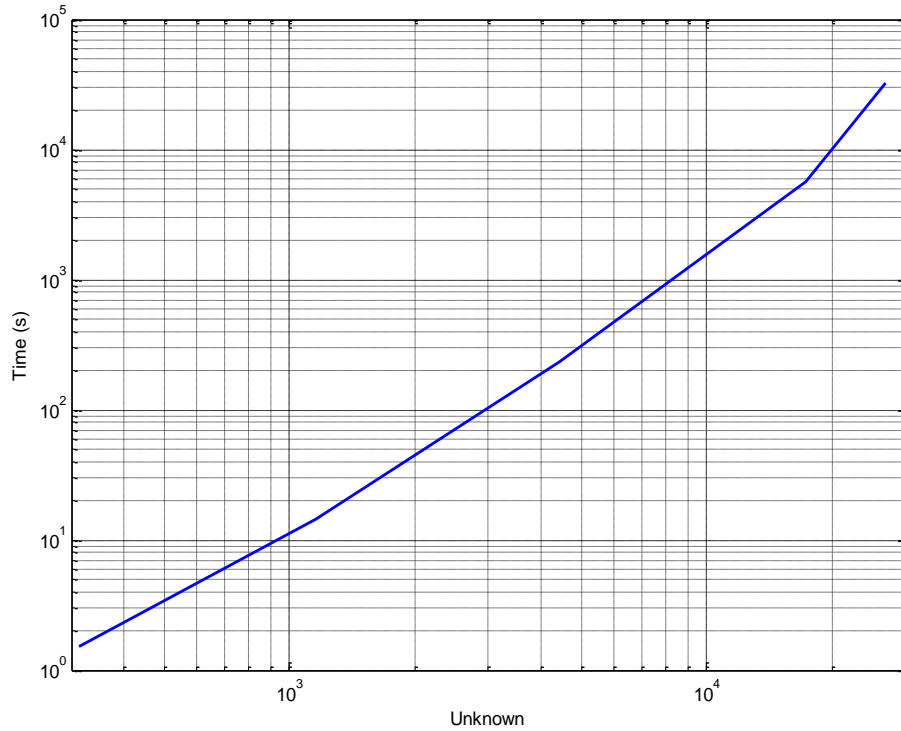
Figure 1.21. Unknowns vs. time

1.1.9. Validation. In order to validate our calculation result, some measurements have benn done. Figure 1.22 shows the test board. It is a two layer PCB. The size is 230 mm 230 mm. The space between two planes is 1.65 mm and the diameter of short via is 2.76 mm.

First, Z11 is measured at the port without short via. The measurement result is shown in Figure 1.23 and the equivalent circuit is shown in Figure 1.24. From this equivalent circuit, the capacitance between two planes and L_{11} can be calculated.

Second, the short via is added and the Z11 is measured again. The measurement result is shown in Figure 1.25 and the equivalent circuit is shown in Figure 1.26. From this equivalent circuit, the mutual inductance M and L_{22} can be calculated.

$$L_{total} = L_{11} + L_{22} - 2M = 5.13nH \tag{1.29}$$

$$L_{plane} = L_{total} - L_{via} = 5.13nH - 606pH = 4.52nH \tag{1.30}$$

Figure 1.22. Test board
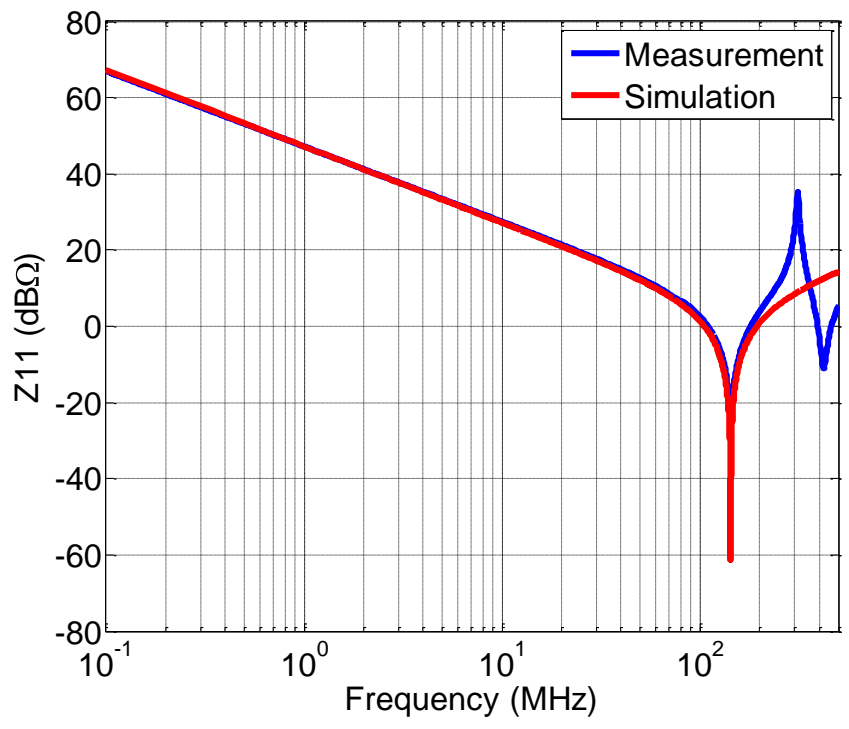
Figure 1.23. Measurement result without short via

Table 1.7 shows the measurement result and calculation results. The calculation results match the measurement result very well. Also from Figure 1.25, it shows that the frequency range for this inductance is up to about 300 MHz. When the frequency is

higher than 300 MHz, the capacitance between plane pair can not be ignored. This method cannot be used anymore.
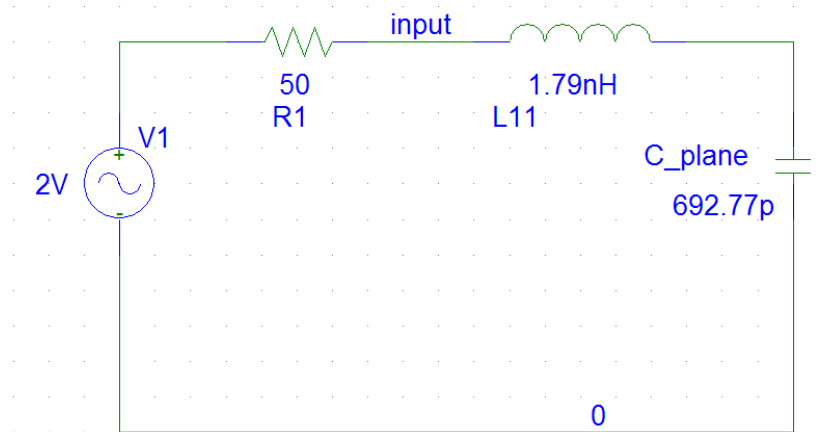
Figure 1.24. Equivalent circuit without short via
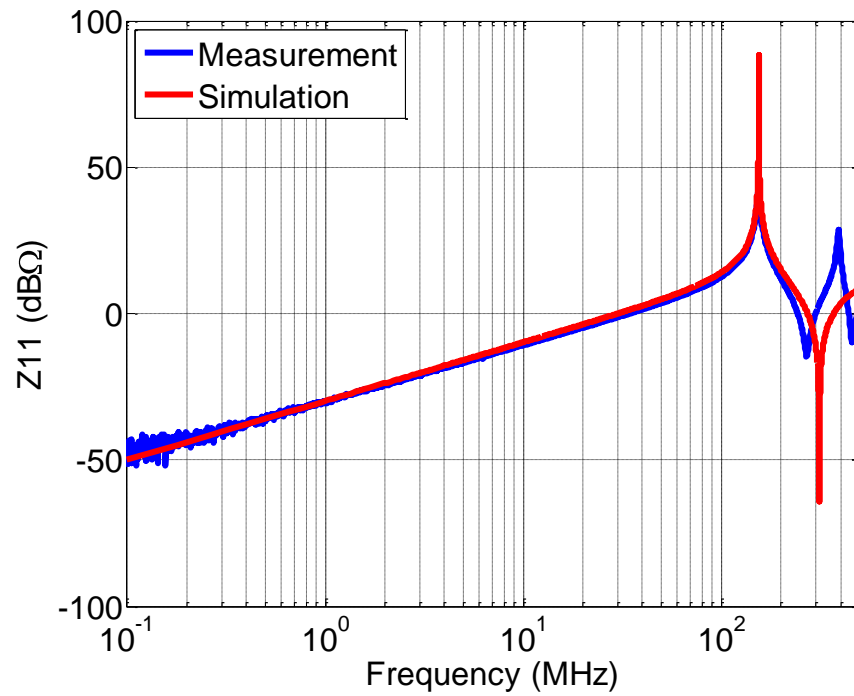
Figure 1.25. Measurement result with short via
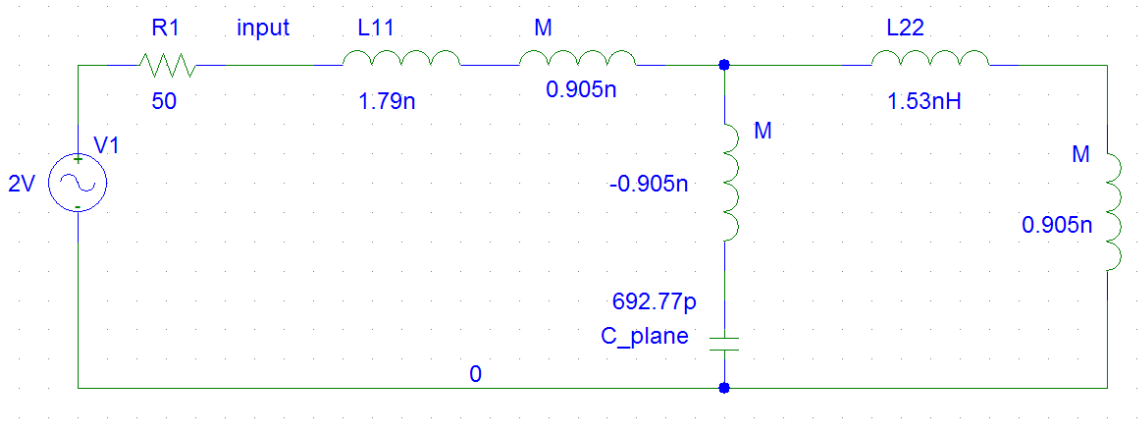
Figure 1.26. Equivalent circuit with short via

Table 1.7. MEASUREMENT AND CALCULATION RESULT

	Measurement	Adaptive Mesh	Hybird
Inductance (nH)	4.52	4.49	4.47

1.5 CONCLUSIONS

The approach introduced in this research for the computation of the Zpp type plane pair inductances is very promising. The new (Ls) PEEC formulation is a special case of the conventional PEEC formulation taking advantage of the opposite currents in the planes. This assumption is the same as is used in the conventional Zpp computation. The approach is much more efficient since the circuit matrix can be simplified and made sparse without loss of accuracy. A sparse matrix solver can be used to further reduce the compute time. The approach is suitable for the optimization of decoupling capacitor placement. As is shown in this research, the computation for different decoupling capacitors can be achieved with only small changes in the MNA matrix.

1.6 REFERENCES

1. M. Zhao, R. V. Panda. S. Sachin. S. Sapatnekar and D. Blaauw, "Hierarchical analysis of power distribution networks," IEEE Trans. Computer Aided Design, vol. 21, No. 2, pp. 159-168, Feb. 2002.

2. A. E. Ruehli, G. Antonini, J. Esch, J. Ekman, A. Orlandi and A. Mayo, "Nonorthogonal PEEC formulation for time and frequency domain EM and circuit modeling," IEEE Trans. Electromagn. Compat. Vol. 45, no. 2, pp. 167-176, May 2003.

3. J. Kim, J. Kim, L. Ren, J. Fan, J. Kim, and J. L. Drewniak, "Extraction of Equivalent Inductance in Package-PCB Hierarchical Power Distribution Network," IEEE 18th Conference on Electrical Performance of Electronic Packaging and Systems, Oct.2009.

4. A. E. Ruehli, C. Paul, and J. Garrett, "Inductance calculations using partial inductances and macromodels," in Proc. of the IEEE Int. Symp. On Electromagnetic Compatibility, pp. 23-28, Atlanta, GA, August 1995.

5. P. K. Wolff and A. E. Ruehli, "Inductance Computations for Complex Three Dimensional Geometries," Int. Symp. On Circuits and Syst, (ICCAD), Chicago, Il, pp. 16-19, 1981.

6. A. E. Ruehli, "Inductance calculations in a complex integrated circuit environment," IBM Journal of Research and Development, 16(5).pp. 470-481, September 1972.

7. Brian Young, Digital Signal Integrity Modeling and Simulation with Interconnects and Packages, Prentice Saddle River, NJ, 2001.

8. PowerPEEC, was provided by Bruce Archamebault, IBM Raleigh, NC.

2. MEASURING IV SWITCHING CURRENT WAVEFORMS USING A GMI PROBE FOR POWER INTEGRITY STUDIES MEASURING IC

Fan Zhou, Fan Jun, David Pommerenke

Electrical Engineering

Missouri University of Science and Technology, Missouri, U.S.A 65401

Email: fzm73@mst.edu, davidjp@mst.edu, jfan@mst.com

2.1 ABSTRACT

IC switching current is the main noise source of many power integrity issues in printed circuit boards. Accurate measurement of the current waveforms is critical for an effective power distribution network design. In this research, using a giant magneto-impedance (GMI) probe for this purpose is studied. A side-band detection and demodulation system is built up to measure various time-domain waveforms using an oscilloscope. Improvements in the probe design, including a balanced circuit for increased signal to noise ratio and an on-probe magnetic-field bias circuit, are proposed. These improvements in the probe design make the GMI probes more suitable for practical applications of time-domain transient current measurements. It is found that the GMI probes are potentially suitable for this kind of time-domain measurements, but probe designs and measurement setups need further improvements for this application.

Keywords

GMI, Time-domain measurement

2.2 INTRODUCTION

In many EMC applications, knowledge of current is essential. For example, IC switching current is necessary for an effective power distribution network design. The conventional design criterion of target impedance can only be accurately specified when the waveform of the IC switching current is known. In ESD investigations, the distribution of the ESD current in the device under test is the key to the understanding of the coupling physics and failure mechanisms. There are many other occasions that an accurate measurement technique is desirable to obtain the time-domain current waveforms.

Generally speaking, magnetic-field loop probes are very suitable for current measurements and are commonly used in many applications. Sensitivity, spatial resolution, and frequency range are all related to the probe structure. In most cases, compromise has to be made in loop probe designs to achieve the most suitable probe performance for the specific application. In addition, for time-domain current measurements, the response of the loop probes is the derivative of the current to be measured. Therefore, a de-convolution procedure is required to obtain current waveforms from the induced voltage waveforms, which may not be trivia due to the noise present in the measurement system.

Magnetic probes can be effectively used for current measurements. These probes need to have a high sensitivity, a high spatial resolution, and a wide frequency range, especially for time-domain measurements where the dynamic range of an oscilloscope is much smaller than a typical spectrum analyzer and the requirement for signal-to-noise ratio is much higher since a wide frequency band is involved.

In terms of sensitivity and miniaturization, giant magneto-impedance (GMI) sensor in a thin-film form has excellent performance. High sensitivity in the order of 10-12 T has been reported in [1]. The GMI sensor is designed based on the skin effect and permeability change of a soft magnetic material when it is exposed to an external magnetic field. Usually the change is more significant close to certain magnetic resonances. Previous research also reveals that the GMI sensor can remain highly

sensitive in a wide frequency range from 5 kHz to 1 GHz without jeopardizing its spatial resolution [2].

In this study, a probe with a thin-film GMI sensor (element) is used to measure time-domain waveforms using an oscilloscope. A sideband detection and demodulation circuit is designed and implemented. Then some improvements are made in the probe design, including a balanced circuit for increased signal to noise ratio and an on-probe magnetic-field bias circuit, are proposed. These improvements in the probe design make the GMI probes more suitable for practical applications of time-domain transient current measurements. The unique contribution of this work involves the extension of the previous GMI study to the time domain, which is much more challenging since the requirement for signal-to-noise ratio significantly increases.

2.3 GMI PROBE

2.3.1 GMI Probe Structure. A GMI probe, as shown in Figure 2.1, is used in this study. It is comprised of a thin-film GMI sensor at the tip and two 85 Ω microstrip traces with SMA connectors for cable connections. The GMI sensor includes a multilayer magnetic strip, which is deposited by RF sputtering on a 1 mm-thick glass substrate with a dielectric constant of 5.8. The stack-up of the magnetic strip is Ta(5)/[NiFe(100)/Cu(5)]*9/NiFe(100)/Ta(5), where the numbers in parentheses are layer thicknesses in nm and *9 means there are 9 repetitive layer pairs. The length of the magnetic strip is 1000 μm and the width is 5 μm. A pair of copper electrodes with a thickness of 1 μm is formed at both ends of the magnetic strip by dc sputtering. The details of the GMI sensor are illustrated in Figure 2.2 [3].

Figure 2.1. Overall view of GMI probe

2.3.2 DC Magnetic Field. A carrier at 1 GHz is fed into the GMI probe. When the GMI sensor is in a time-varying external magnetic field, the field interacts with the GMI sensor and creates a sideband through amplitude modulation. Then, the strength of the magnetic field at the location of the GMI sensor can be measured from the sideband magnitude in the GMI probe output.

The skin-effect and the permeability of the GMI sensor change with the external magnetic field, and further there are regions where the rate of the changes is larger than elsewhere [3]. In other words, under some dc bias, the GMI probe can be more sensitive to time-varying ac magnetic fields. To find a suitable dc magnetic field bias, the |S21| of the GMI probe as a function of the dc external magnetic field was examined first. The GMI sensor was placed in the center of a Helmholtz coil and was thus subject to a dc external magnetic field, sweeping from -15 Oe to 15 Oe. The direction of the dc magnetic field is parallel to the longitudinal direction of the GMI sensor. The test configuration is showed in Figure 2.3.

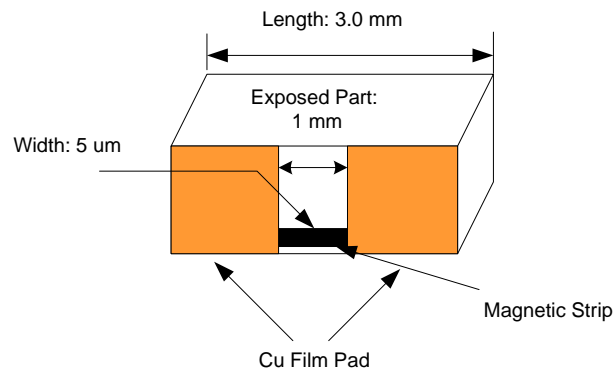

Figure 2.2. Illustration of GMI sensor

The measured |S21| results as a function of the dc magnetic field strength are plotted in Figure 2.4. For this particular GMI sensor, the stronger the dc magnetic field is, the higher the insertion loss. As mentioned earlier, to achieve the highest sensitivity, the

dc bias point needs to be set at the location where the slope of the curve is the largest. In this study, the dc bias is chosen to be 10 Oe.
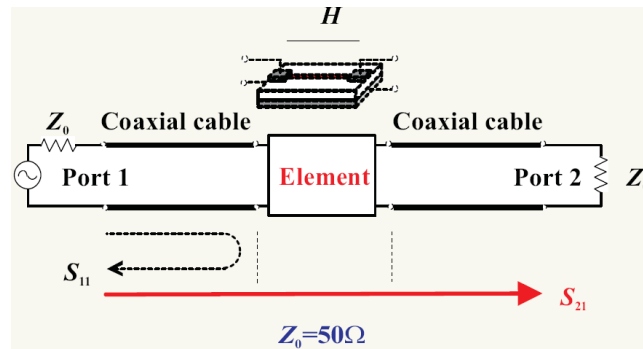
Figure 2.3. Experimental setup for dc magnetic field bias

2.3.3 Characterization of the Probe. In order to validate the measurement setup, the GMI probe was used to measure the magnetic field radiated from a microstrip trace in the frequency domain first, as shown in Figure 2.5. Three cases were studied with the 50 Ω microstrip trace terminated with a short circuit, a 50 Ω matched load, and an open circuit, respectively. The trace was excited with a 5 V peak-to-peak sinusoidal wave with a frequency varying from 200 KHz to 100 MHz. The carrier fed into the GMI probe had a magnitude of 7 dBm. The GMI probe was placed in the middle of the trace. The lower sideband in the probe output was measured.

The power of the lower sideband as a function of the excitation frequency for the three different termination conditions is shown in Figure 2.6. When the trace is shorted at the load RL, the magnetic field from the trace reaches the maximum and the electric field reaches the minimum nearly everywhere along the trace since it is electrically short. On the other hand, when the trace is open-ended, the magnetic field from the trace is the minimum while the electric field is the maximum. From Figure 2.6, the sideband power for the open-ended case is at least 20 dB lower than the short-ended case. This demonstrates that the magnetic field coupling dominates over the electric field coupling in the GMI probe, and thus further validates the measurement setup.
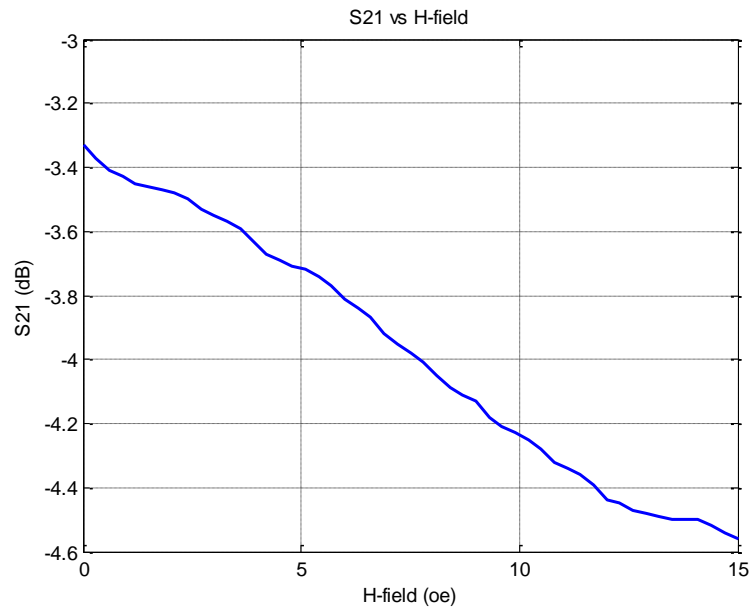
Figure 2.4. $|S_{21}|$ versus dc magnetic field strength
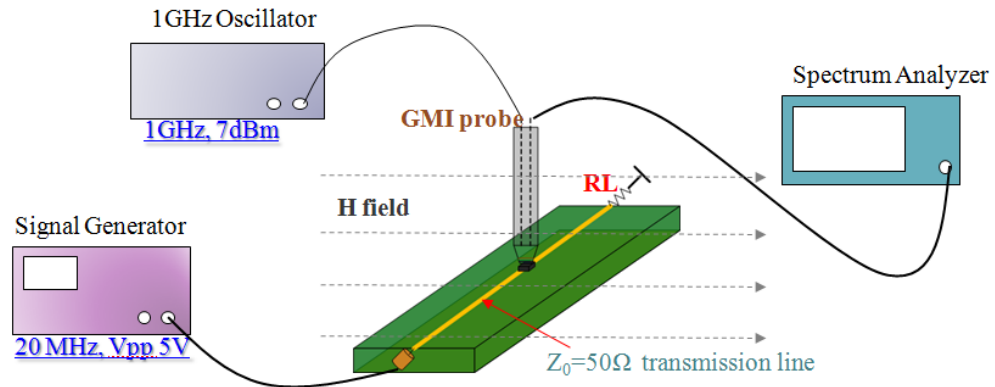
Figure 2.5. Measuring magnetic field from trace in the frequency domain

It can also be observed that the output power of the lower sideband remains approximately the same at different frequencies for the 50 Ω matched load condition. In other words, the frequency response of the GMI probe is approximately flat in the frequency range under study. This is a significant advantage of the GMI probe compared with the conventional loop magnetic field probe in time-domain measurements. Because

of its flat frequency response, the GMI probe potentially can directly reproduce the time-domain waveforms under test without any de-convolution procedure. Further, it may measure low-frequency magnetic fields more effectively than the loop probes where the sensitivity is proportional to frequency.
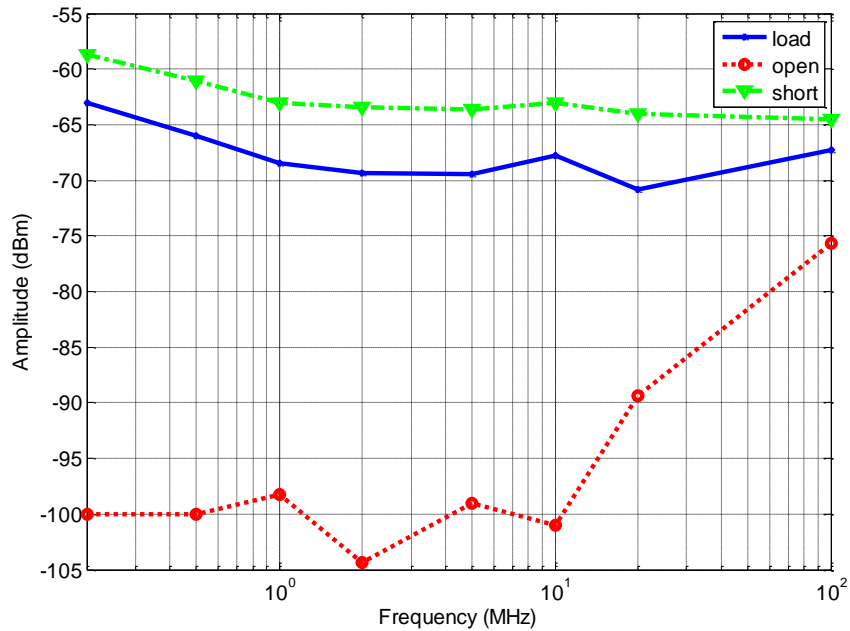
Figure 2.6. Measured power of lower sideband versus excitation frequency

2.3.4 Time-domain Waveform Measurements. To measure the time-domain waveforms using the GMI probe and an oscilloscope, the measurement setup shown in Figure 2.5 was further developed to include sideband detection and demodulation. A mixer was used to down convert the sideband to reproduce the trace current under measurement. Since the sideband power was very low and the carrier component was strong, several stages of amplification and low-pass filtering were needed. The improved experimental setup is illustrated in Figure 2.7.
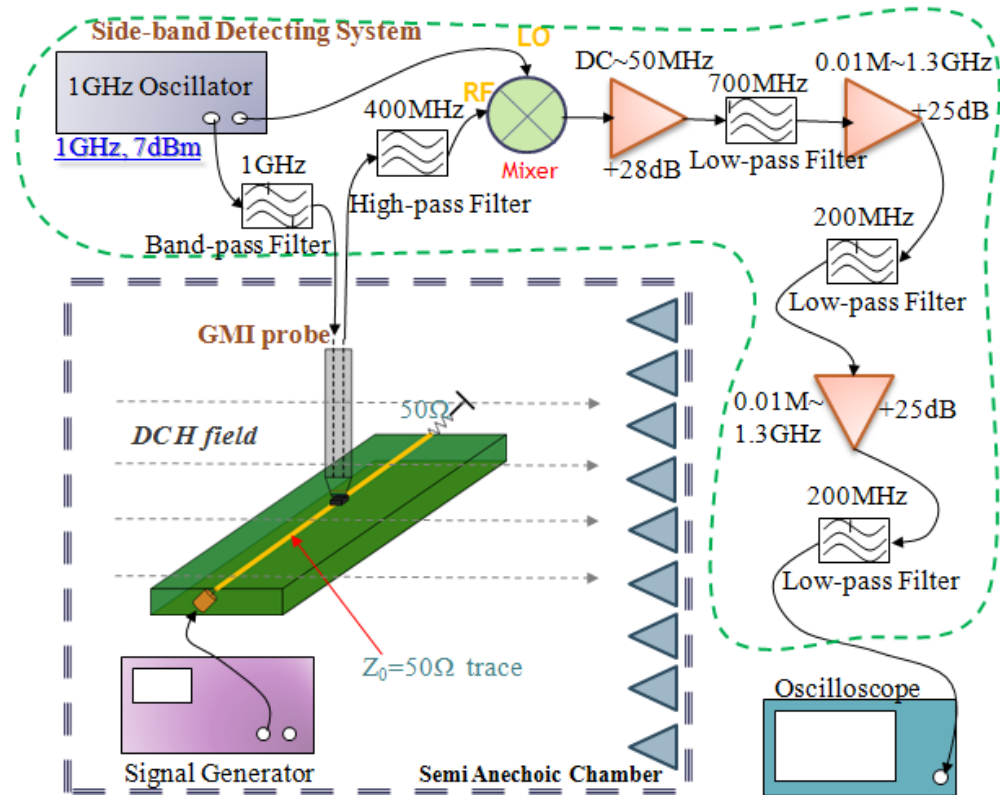
Figure 2.7. Improved setup for time-domain waveform measurements

In this design, the oscillator module generated two identical 1 GHz, 7 dBm sinusoidal signals. One signal served as the carrier and was fed into the GMI probe, which was place in a semi-anechoic chamber. The other oscillator signal was used as the local oscillator for the mixer. The 50 Ω microstrip trace was excited with various time-varying waveforms, and the magnetic field from the trace was picked up by the GMI sensor and was further modulated with the 1 GHz carrier. The output of the probe, which included the modulated signal, was then fed into the mixer. The output of the mixer contained the wanted de-modulated signal as well the unwanted carrier and sideband signals. Unfortunately the wanted signal was more than 80 dB lower in power than the unwanted ones. Therefore, a dc to 50 MHz first stage amplifier was used to amplify the wanted signal only. The narrow band of this amplifier could help increase the signal-to-noise ratio. Then a 700 MHz low-pass filter was used to attenuate the unwanted signals.

Following this, another two stages of amplification and filtering were also included in order to raise the power ratio of the wanted to the unwanted signals.

There was a 1 GHz band-pass filter, applied right before the carrier signal went into the probe. It was used to prevent the noise due to the electric field coupling from the GMI probe, which was not carefully designed for electric-field shielding, from propagating into the oscillator and from further creating modulated noise. For similar considerations, a 400 MHz high-pass filter was used right after the output of the GMI probe in order to prevent the noise due to the electric field coupling from propagating into the mixer.

The DUT was placed into a semi-anechoic chamber to prevent the coaxial cables used in the sideband detection and demodulation system from picking up the radiated noise from the microstrip trace.

2.3.5 Measurement Results. Different waveforms were used to excite the microstrip trace, including a 20 MHz, 5 V peak-to-peak sinusoidal wave, a 10 MHz, 5 V peak-to-peak rectangular wave with a 50% duty cycle, and a 15MHz, 5 V peak-to-peak pulse train with a rise/fall time of 10 ns and a pulse width of 12.5 ns.

The measured waveforms for the sinusoidal excitation are shown in Figure 2.8. The upper waveform is the one measured by the GMI probe. The lower one is obtained from the direct measurement of the trace load voltage (i.e., the trace current multiplied with 50 Ω), as a reference. The two waveforms are very similar with a phase shift, which is caused by the difference in cable delays. The measured peak-to-peak magnitude from the GMI probe is approximately 0.6% of the reference voltage. In other words, the transfer coefficient of the GMI probe is approximately 0.3.

The measured waveforms for the rectangular excitation are shown in Figure 2.9. They are almost the same except at the rising and falling edges. Since the bandwidths of the amplifiers and filters in the measurement setup are limited, the higher frequency spectrum associated with the edges cannot be fully measured by the GMI probe. The transfer coefficient of the GMI probe remains at approximately 0.3.

The measured waveforms for the pulse train excitation are shown in Figure 2.10. The waveform captured by the GMI probe looks similar to the reference one, with exactly the same period. But the details at the sharp edges are not well captured, again

because of the bandwidth limitation of the amplifiers and the filters. The transfer coefficient of the GMI probe in this case is approximately 0.35, slightly off from the previous two cases. This inaccuracy is probably caused due to the loss of the high-frequency spectral information.
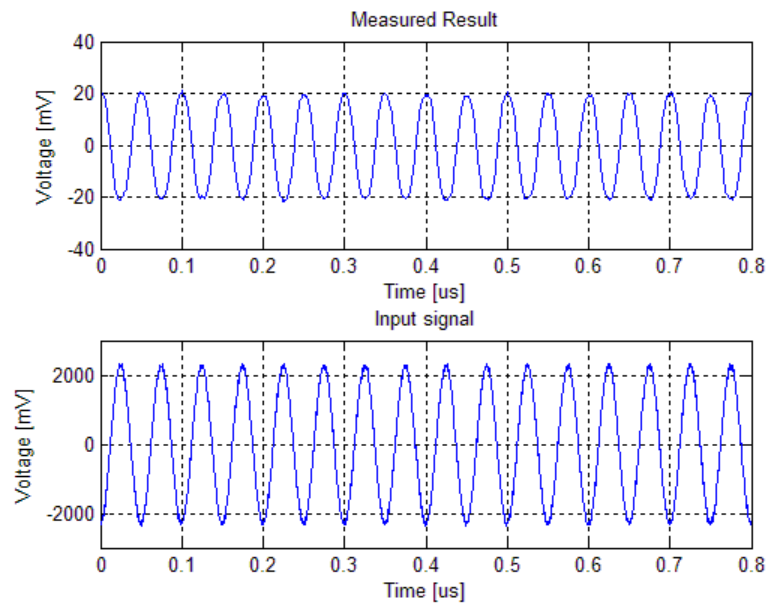

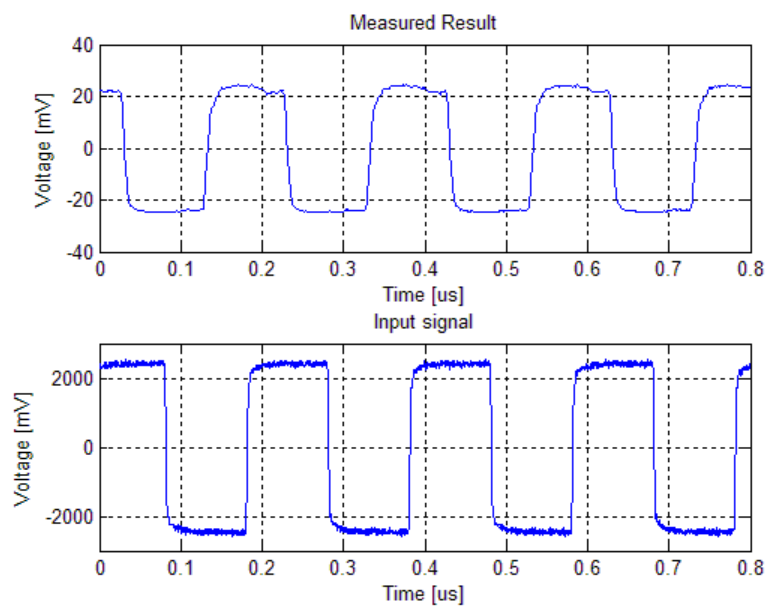Figure 2.8. Measured waveforms for the sinusoidal excitation

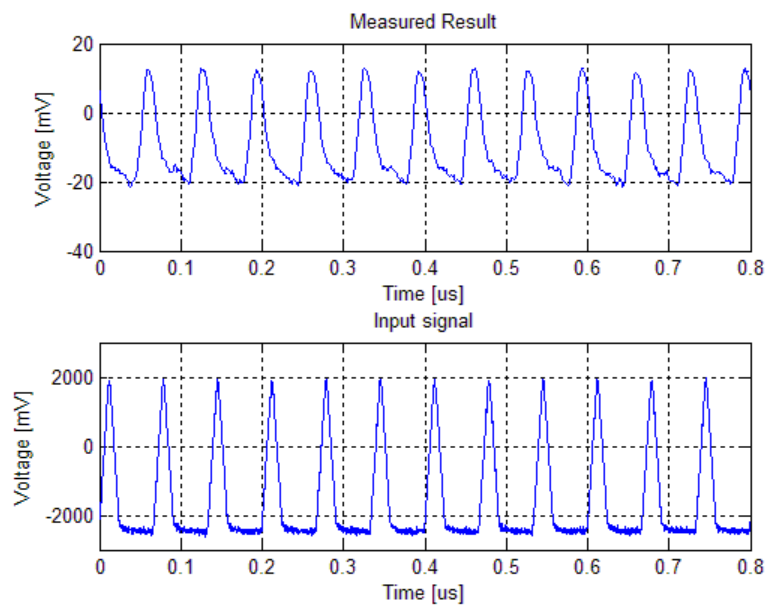Figure 2.9. Measured waveforms for the rectangular excitation

Figure 2.10. Measured waveforms for the pulse train excitation

2.4 IMPROVED TIME-DOMAIN WAVEFORM MEASUREMENT SETUP

Although time-domain waveforms were re-produced using a sideband detection and demodulation system, performance was not sufficient for typical transient current measurements. Further, the Helmholtz coils used to provide the dc magnetic field limited DUT's size and geometry, and they could cause potential measurement errors. Therefore, improvements in the probe design are proposed in this research to deal with these issues.

2.4.1 On-probe Magnetic Field Bias. The dc magnetic field is needed to set the GMI element to work at a highly sensitive point. In order to supply a dc magnetic field in the magnitude of 10 Oe, Helmholtz coils with a diameter of 10 cm were used. As discussed earlier, the external Helmholtz coils are not practical for real-world EMC measurements.

To make the GMI probes more suitable for practical applications, the dc magnetic-field bias is proposed to be provided locally in the probe PCB design. A simple while effective solution is to use a large via drilled very close to the GMI sensor. When a dc current runs through the via, the generated dc magnetic field can be used as a local bias for the GMI sensor. And the magnitude of this dc magnetic field can be easily tuned by changing the dc current. This proposed structure is illustrated in Figure 2.11.

Experimental validation of the on-probe magnetic-field bias circuit shows that the dc magnetic field provided by the dc current flowing through the via does bias the GMI sensor at the suitable working point. The same level of the sideband magnitude is achieved as using the external Helmholtz coils.

The advantages of the on-probe magnetic-field bias circuit include the localized magnetic field that attenuates quickly so that this bias field only imposes negligible effects on the DUT. Further, it removes the requirement to have external setups that significantly limit the applications of the GMI probe.
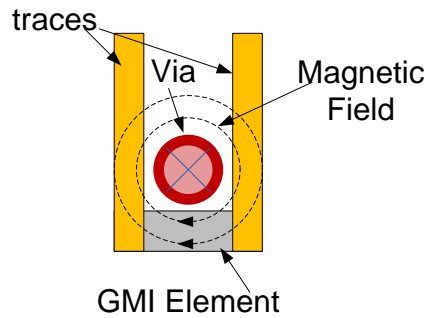
Figure 2.11. On-probe dc magnetic field bias using a local via

2.4.2 A Balanced Circuit to Improve Signal to Noise Ratio. In the magnetic field measurements in the frequency domain using a GMI probe, the sidebands can be directly measured using a spectrum analyzer with a very good accuracy as long as the sidebands are away from the carrier. However, to further get the time-domain current waveforms, demodulation is necessary and the overall signal to noise ratio of the system plays a critical role in this step. With the original GMI probe design, the dominant signal spectrum at the probe output includes the carrier frequency and the two sidebands of the modulated signal. Often the power of the carrier frequency is 70 dB or 80 dB higher than that of the modulated signal. This greatly limits what can be done to increase the overall signal to noise ratio of the measurement setup.

A balanced circuit is proposed in this research to suppress the carrier frequency in the GMI output, so that changes can be made in the measurement setup to increase the signal to noise ratio. The schematic of the proposed circuit is shown in Figure 2.12. The dc resistance of the GMI sensor changes from 38.5 Ω to 38.8 Ω with different magnetic-field bias values. A 39 Ω resistor is connected in series with the GMI element to create a balanced circuit. The carrier signal, split into a pair of differential inputs (equal magnitude but out of phase), is fed into the GMI element via two equal-length traces. In this way, at the output node, which is between the GMI element and the resistor, weak carriers signal but relatively strong sidebands are generated.

Differential input

+   -
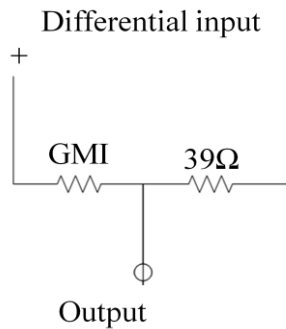
GMI   39Ω

Output

Figure 2.12. The schematic of the proposed balanced probe design

A hybrid, as shown in Figure 2.13 is used to generate the differential carrier signal inputs. Theoretically, with perfectly balanced probe and trace design, the carrier signal can be ideally eliminated. But in practice, the carrier signal can still be observed in the GMI probe output, because the lengths of the traces and cables are not exactly equal and the trace impedance (85 Ω) does not match with the load impedance (50 Ω). Using the balanced circuit topology by revising the original probe design in the lab, the power of the carrier signal at the output node is measured to be -11 dBm, which is much smaller than that using the original circuit topology (approximately 2.25 dBm). At the same time, the sideband power increases from approximately -70 dBm to -65 dBm, due to the increased sensitivity of the balanced circuit for detecting small resistance changes.

With the decrease of the carrier power, it becomes possible to use a low noise amplifier right after the GMI probe output to increase the signal-to-noise ratio of the measurement system. This was not possible when the carrier power was high, since the carrier signal could easily saturate the amplifier. The rest of the measurement setup is shown in Figure 2.13. In this improved setup with the low noise amplifier, only one amplifier and one low-pass filter are needed after the down mixer to obtain the signals suitable for oscilloscope measurements. In the previous setup, multiple stages of amplifications and filtering were necessary, and the resulting signal to noise ratio was still smaller.

The benefits of the balanced circuit are two folds. First, it significantly reduces the carrier power so that a low noise amplifier can be added right after the GMI output,

which greatly increases the signal to noise ratio. Secondly, a balanced circuit is more sensitive to the small changes of resistance. As a result, the sideband power increases in the balanced design.

A bridge circuit can also be used instead of the simple balanced circuit shown in Figure 2.12. However, the bridge circuit may introduce a loop, which can respond to magnetic field as well, resulting in potential measurement errors.
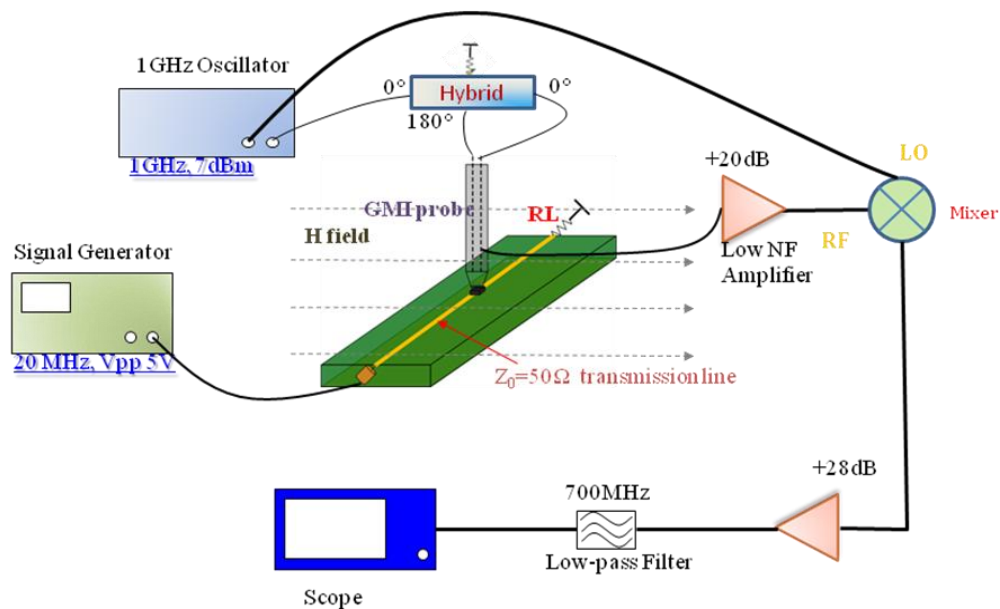
Figure 2.13. Improved setup for time-domain transient current measurements

2.5 IMPROVED TIME-DOMAIN WAVEFORM MEASUREMENTS

In order to test the effectiveness of the improved probe design and measurement setup, different waveforms are measured using the GMI probe as shown in Figure 2.13, including a 20 MHz 10 V peak-to-peak sinusoidal wave, a 10 MHz 5 V peak-to-peak pulse train with a rise/fall time of 10 ns and a pulse width of 12.5 ns, and a 50 MHz 5 V peak-to-peak pulse train with a rise/fall time of 10 ns and a pulse width of 12.5 ns. These

input voltage waveforms are used to excite the 50 Ω microstrip trace, which is terminated with a matched load.

The measured voltage waveforms for the sinusoidal excitation are shown in Figure 2.14, where the top plot shows the demodulated GMI output and the bottom one shows the measured voltage at the trace load. Notice that the trace current can be directly calculated from the load voltage through Ohm's law; therefore, the bottom plot provides a reference for the trace current to be measured by the GMI probe. It can be seen from the figure that the two waveforms are very similar with a phase shift, which is caused by the difference in cable delays. The measured peak-to-peak magnitude using the GMI probe is approximately 0.32% of the reference voltage. In other words, the transfer coefficient of the overall measurement setup is approximately 16%.

The measured waveforms for the 10 MHz pulse train excitation are shown in Figure 2.15. The demodulated GMI output waveform is almost the same as the reference voltage waveform except at the rising and falling edges, indicating that the overall bandwidth of the measurement setup is limited and the higher frequency spectrum components associated with the edges cannot be fully captured by the measurement setup. The measured peak-to-peak magnitude using the GMI probe is also approximately 0.32% of the reference voltage in this case.

The measured waveforms for the 50 MHz pulse train excitation are shown in Figure 2.16. It can be seen from the figure that the demodulated GMI output waveform looks very similar to the reference one, with exactly the same period. But, the details at the sharp edges are not well captured, again because of the bandwidth limitation of the measurement setup. The measured peak-to-peak magnitude using the GMI probe is approximately 0.32% of the reference voltage. Again, this indicates that the transfer coefficient of the entire measurement setup is approximately 16%.
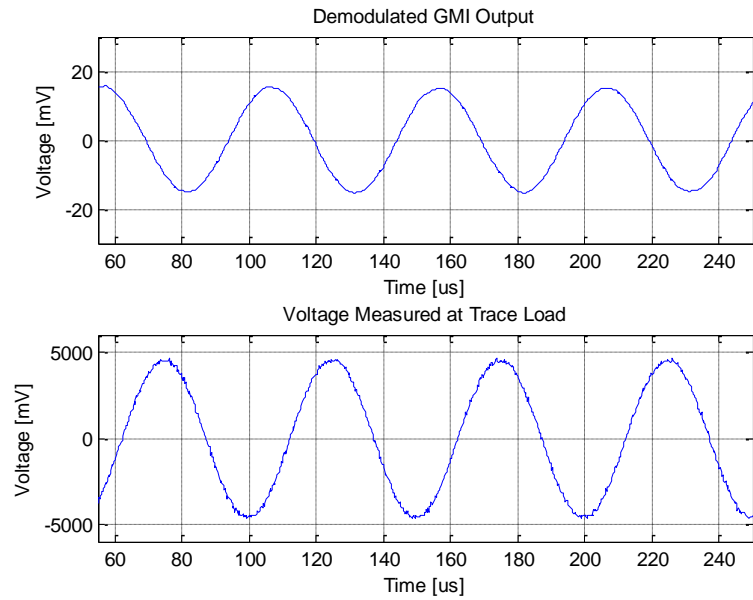
Figure 2.14. Measured waveforms for the 20 MHz sinusoidal excitation
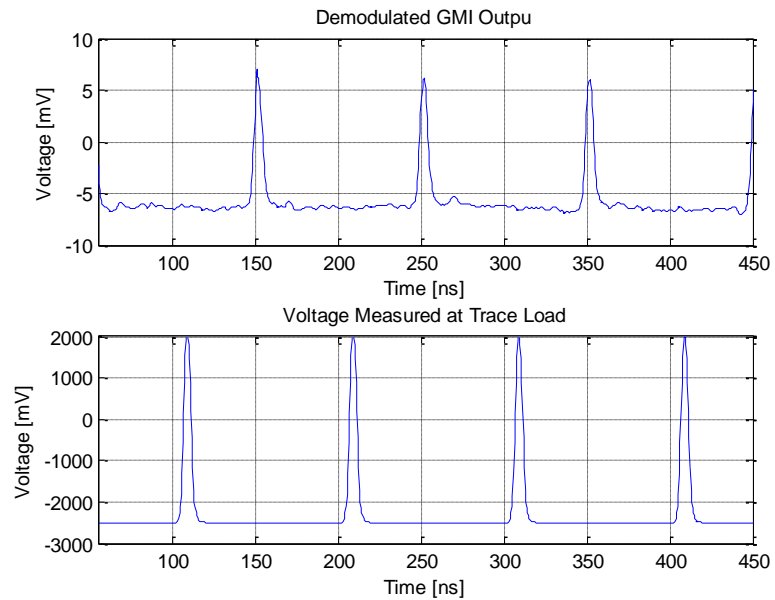
Figure 2.15. Measured waveforms for the 10 MHz pulse excitation
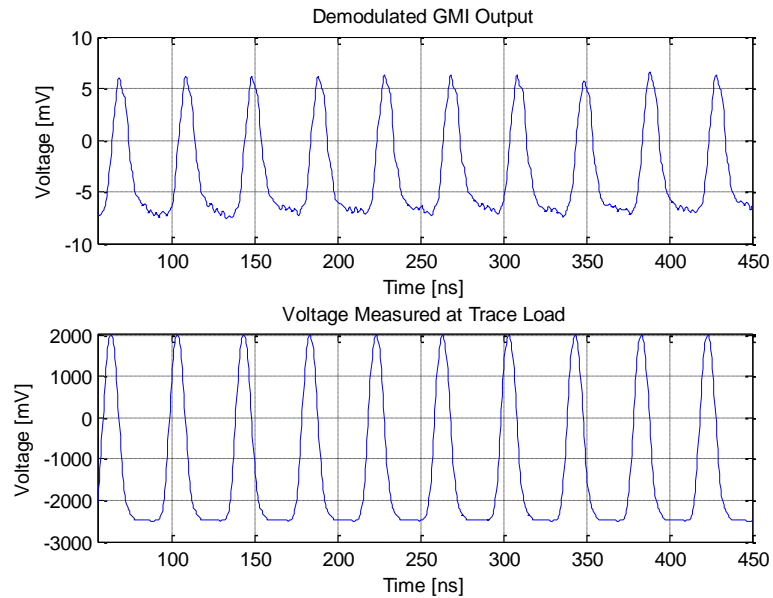
Figure 2.16. Measured waveforms for the 50 MHz pulse excitation

2.6 CONCLUSIONS

The GMI probes have a great potential in various time-domain transient current measurements. They have a high sensitivity to magnetic field, a good spatial resolution, and a wide frequency range. The response of the GMI probes to magnetic field is approximately frequency independent, which is particularly useful for time-domain current measurements.

The improved probe design proposed in this paper makes the GMI probes more suitable for practical time-domain EMC applications. The balanced circuit topology significantly reduces the carrier power and at the same time increases the sideband power. Thus, a low noise amplifier can be added right after the GMI output to significantly increase the signal to noise ratio of the measurement setup. The on-probe magnetic-field bias circuit provides a localized dc magnetic field to bias the GMI sensor to a suitable working point, while reduce the potential interference of the dc magnetic field with the DUT. Further, it eliminates the need of external Helmholtz coils or permanent magnets, greatly simplifying the measurement setup.

With the improved probe design and measurement setup, several examples of trace current with either a sinusoidal or pulse train waveform have been successfully reproduced in the oscilloscope, demonstrating the effectiveness of the improvements proposed in this paper.

Future research directions in this topic include other improvements to the probe design, such as rejection to electric-field coupling and improved carrier suppression, increased bandwidth of the measurement system, and improvements in the GMI sensor for increased sensitivity.

2.7 REFERENCES

1. H. Kikuchi, S. Yabukami, M. Yamaguchi, K. I. Arai, and T. Suzuki "High sensitive detection of ac magnetic field using high-frequency carrier-type thin-film magnetic field sensor with carrier-suppressing circuit," J.Magn.Soc.Jpn., vol 26, pp. 562-565, 2002.

2. K.Tan, K. Yamakawa, T. Komakine, M. Yamaguchi, Y. Kayano, and H. Inoue, "Detection of wide band signal by a high-frequency-carrier type magnetic probe," J. Appl. Phys., vol. 99, 08B315, 2006.

3. F. Zhou, S. Wu, D. Pommerenke, Y. Kayano, H. Inoue, K. Tan, and J. Fan, "Measuring IC switching current waveforms using a GMI probe for power integrity studies," accepted to be published in the 2010 Asia-Pacific Symposium on Electromagnetic Compatibility, Beijing, China, April 12-16, 2010.

4. K. Tan, M. Yamaguchi, K. Yamakawa, K.Ocuchi, and K.I. Arai "Micro-Size Magnetic Strip for Ultra High Frequency carr ̄ , ier Type Magnetic Field Sensor," IEEE Transactions on Magnetics, vol. 37, No.4, pp 2004-2006, July 2001.

SECTION

1. **NEW RULE FOR EVALUATING CONDUCTOR SURFACE ROUGHNESS**

1.1 INTRODUCTION

Accurate characterization of printed circuit board (PCB) laminate dielectric materials is an important problem for high-speed digital designers and signal integrity (SI) engineers [1]. It is desirable to be able to extract dielectric constant (Dk) and loss tangent, or dissipation factor (Df) in a wide frequency range from at least a few MHz to about 50 GHz. Wideband travelling-wave methods of S-parameter measurements "in situ" on PCB test vehicles can be realized in either frequency domain or in time domain. Frequency-domain methods use vector network analyzers (VNA) [2], while time-domain methods can be realized either using time-domain reflectometers (TDR) [3], or short-pulse propagation (SPP) techniques [4]. Port effects could be removed effectively using TRL calibration techniques either in frequency-domain (f-TRL calibration), or in time-domain (t-TRL calibration) [5]. Figure 1.1 shows a layout of the test boards and TRL calibration pattern.
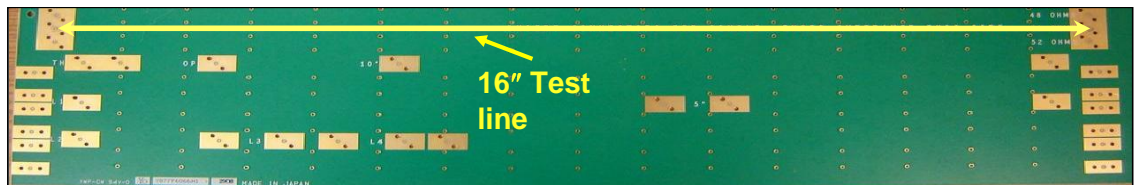

Figure 1.1. Test vehicle for dielectric characterization of PCB laminates dielectric

Assuming that there is a single-ended stripline test vehicle to characterize dielectric properties on the PCB substrate, S-parameters directly measured by either

technique can be used to extract the complex propagation constant γ on the line [2]. This complex propagation constant is comprised of the propagation constant β and total loss constant αt on the line,   . In turn, the total loss consists of dielectric and conductor loss parts,   . Though in many cases PCB circuitry designers might be interested in the total loss   in dielectrics, since this loss is responsible for attenuation per unit length on the line and associated frequency dispersion. These effects can be seen, for example, in link path analysis as an eye diagram closure. However, design engineers might need accurate knowledge of dielectric properties Dk and Df over a wide frequency range for choosing correct geometries and evaluating properties of devices or their elements at the design stage. If dielectric loss is not separated correctly from conductor loss, this might lead to further problems of the designs functioning. Separation of dielectric and conductor loss is a real challenge when conductors are significantly rough [6]. For smooth conductors, loss behaves as a square root of frequency $\overline{}$ due to the classical skin effect, but this is not true for rough conductors, especially at frequencies where skin depth is comparable or less than the surface roughness characteristic dimensions. For example, for the widely used in present-day PCB design three major groups of foil (standard – STD, very low profile – VLP, and hyper very low profile – HVLP), conductor roughness might have a significant effect at frequencies of just a few GHz. Frequency contributions of different powers of frequency ($\overline{}$, etc.) could be solely due to rough inhomogeneous conductor surface, and they may lump into the dielectric loss so that the resultant dielectric loss could be overestimated [7]. Thus, it is important to tell dielectric loss contribution apart from the loss on a rough conductor.

There are a number of different analytical and numerical models that allow for estimating conductor loss in a PCB with rough foil and thus get "pure" dielectric loss from the total measured loss [8-19]. However, any existing model requires accurate knowledge on surface roughness profiles. The problem is complicated by the fact that the exact frequency behavior of a dielectric substrate, which is indeed a composite inhomogeneous layered and hence an anisotropic medium, is never available, though some preliminary guess could be made. The new proposed differential extrapolation/redistribution method (DERM) to separate rough conductor loss from dielectric loss also requires knowledge on roughness levels [20].

Currently, the data on the surface roughness could be obtained only through destructive analysis of test samples. This means that pieces of PCB should be cut out and special samples for surface roughness analysis should be prepared. The roughness analysis in industry is typically done using profilometry testing. There are two types of profilometers: mechanical and optical. Optical profilometers are more accurate, since their resolution is typically higher than that of their mechanical counterparts. Figure 1.2 and Figure 1.3 show a surface profilometer and a sample of the surface image obtained using this equipment.

When profilometry of foil surfaces is not available, scanning electron microscopy (SEM) of cross-sections of PCB transmission lines may be a good alternative as shown in Figure 1.4. It is important to develop a method of evaluating surface roughness parameters from SEM pictures and their computerized image processing.

The objective of this research is to present a novel rule, which "Sigma" rule is called to evaluate surface roughness average peak-to-valley amplitude and average period of roughness profile. These numbers would be useful for analytical and numerical modeling, for example, Sanderson-Sundstroem model (SSM) [6, 11, 12]. One of the important problems is to correlate the numbers extracted using this rule with those obtained from the conventional profilometers, as well as from estimation based manual processing of samples of SEM pictures.

1.2 DESCRIPTION OF THE "SIGMA" RULE

First, the test samples of PCB should be prepared for SEM scanning. This requires their cutting out from the PCB test vehicle, whose S-parameters have already been measured using a travelling-wave technique. The sample should be polished, buried in epoxy resin, and after hardening, polished again so that all the features of the trace would be seen clearly. Then the surface under study is coated with a high-conducting (Pt or Au) thin film under vacuum, which is necessary for SEM testing.
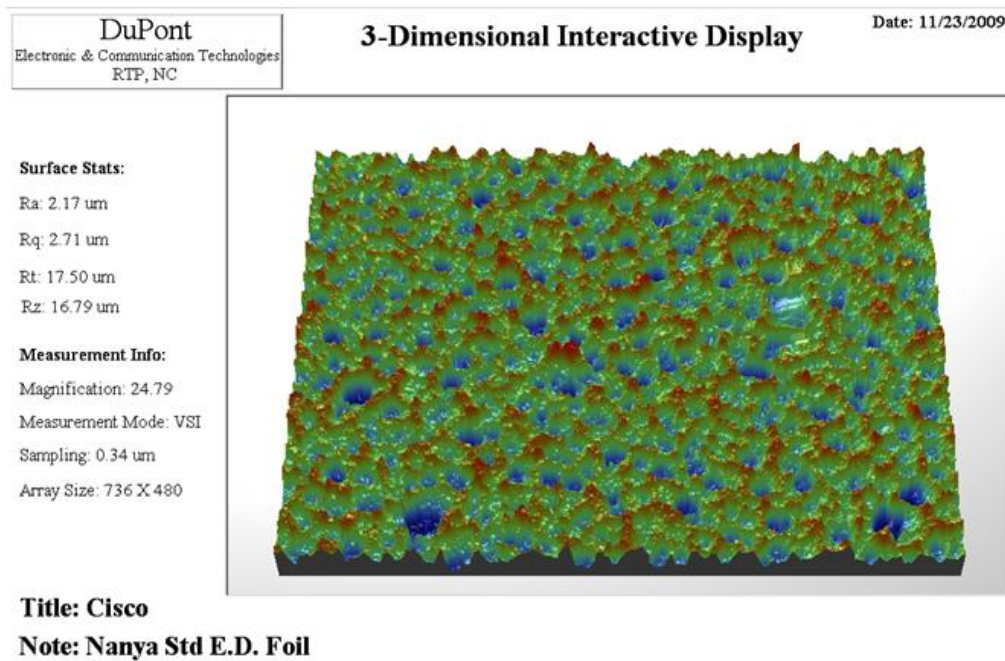
Figure 1.2. Profilometer

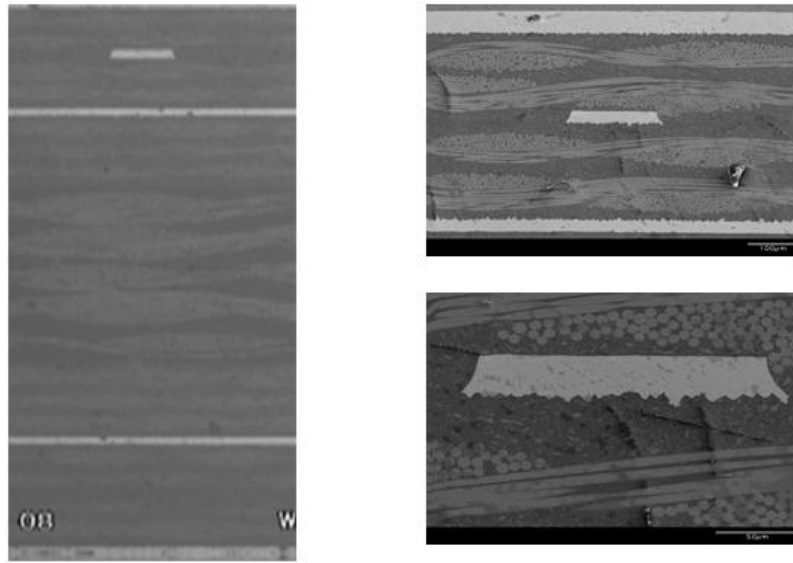Figure 1.3. 3D image obtained by an optical profilometer

Figure 1.4. SEM pictures for stripline under test

The trace surface is typically subdivided into four or more consecutive regions (from left to right), so that both top and bottom surfaces of the selected signal trace are seen, and the corresponding SEM pictures are taken. Then each SEM picture is processed by image-processing software, such as Scion Image, ImageJ, or Photoshop to obtain a continuous high-contrast contour.

If the sample picture was tilted initially, or the sample surface is occasionally inclined, the unwanted linear trend should be removed from the sample image using the Matlab function detrend before including this sample into a total closed line. The resultant sample contours are stitched together in such a way that there would be possibly no overlapping regions. The total contour should be an exact proportional image of the trace.

After the total trace contour is obtained, the corresponding image file (e.g., *.bmp) should be converted to a Matlab figure file, which should show height profile versus corresponding coordinate. This function is called "imread". The mean level on each surface (top or bottom of the trace) should be shifted to the zero level.

When Matlab figure of the roughness profile on the whole trace is available, the Sigma Rule could be applied. If the surface roughness is the Gaussian distribution, the

peak value is 3 times as the cutoff value, and if the surface is exactly the sinewave, the peak value is   as the cutoff cvalue. So 2.2 is chosen. The procedure consists of the following steps for each surface of the trace separately – top and bottom.

1. Since the mean level of the surface is shifted to the zero, the zero line would divide roughness profiles into two regions: upper (positive) and lower (negative). Positive standard deviation   , or average value of everything exceeding the zero level, should be calculated. Then the tolerance of the Gaussian distribution, which equals to 2.2   , should be calculated. This would determine the region where the positive roughness amplitude would lie with the probability of 99%.

2. The same should be done for everything that lies below the zero line. Negative standard deviation   should be calculated as an average of everything that is below the zero level.

3. The resultant peak-to-valley roughness amplitude on either surface would be calculated as   2.2   +|2.2 |.

4. If roughness is different on the top and bottom surfaces of the trace, the greater value of two is considered as the average surface roughness amplitude   .

5. Then the average period of roughness function is evaluated. To do this, the positive cut-off level   and the negative cut-off level   should be drawn.

6. The number of all essential peaks crossing the positive cut-off level should be counted (   ), and the total length of the surface   should be divided by this number to obtain the average positive period   .

7. The same procedure is done for the valleys below the zero level,   .

8. Then the average roughness period can be calculated as. Λ   .

9. If roughness is different on the top and bottom surfaces of the trace, the lower value of two is considered as the average surface roughness period Λ.

1.3 AN EXAMPLE OF SIGMA RULE APPLICATION

Below the proposed "Sigma" rule is demonstrated for calculating roughness parameters of STD foil.

1. Get SEM pictures of different section of the trace as Figure 1.5.
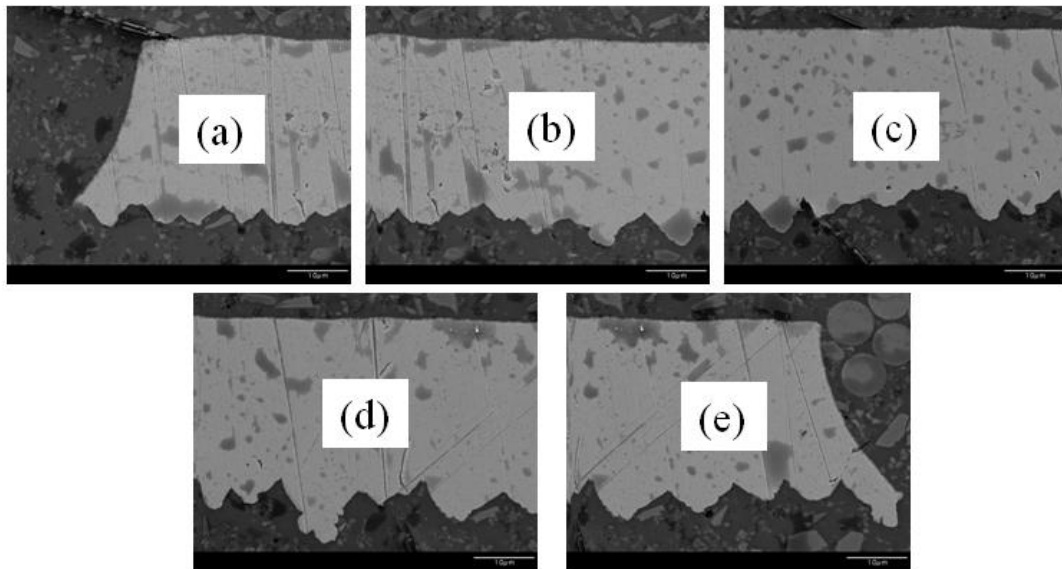

Figure 1.5. SEM pictures of a few consecutive pieces of the signal trace (STD foil)

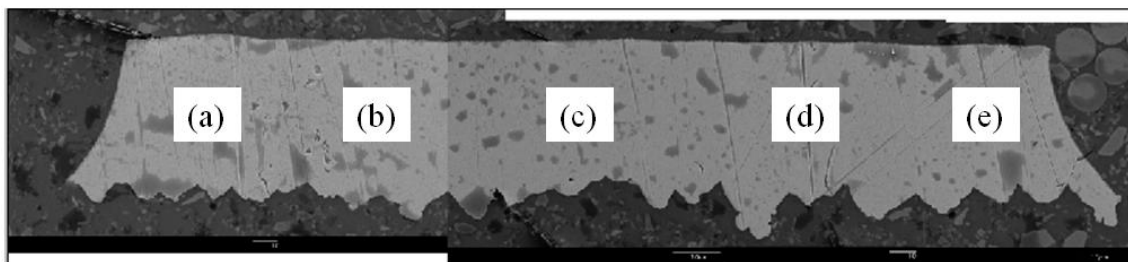2. Obtain a continuous picture as Figure 1.6.

Figure 1.6. SEM pictures of all consecutive pieces of the trace combined together

3. Get bitmap file from SEM picture as Figure 1.7.
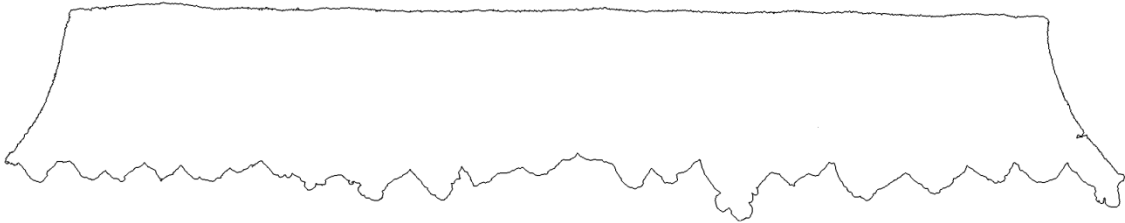

Figure 1.7. Bitmap picture

4. Get trace contour as Figure 1.8.

Figure 1.8. Lower surface contour

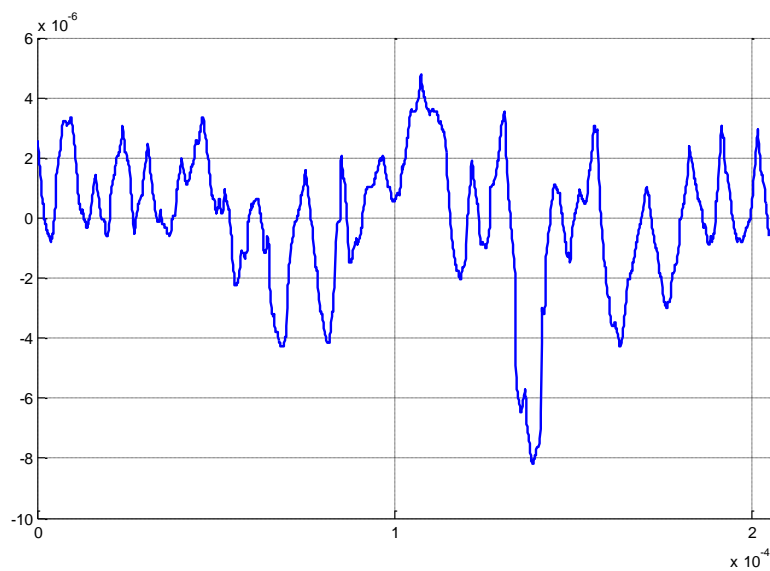5. Convert to a Matlab figure file by "imread" function. The result is shown in Figure 1.9.

Figure 1.9. Roughness profile in Matlab file

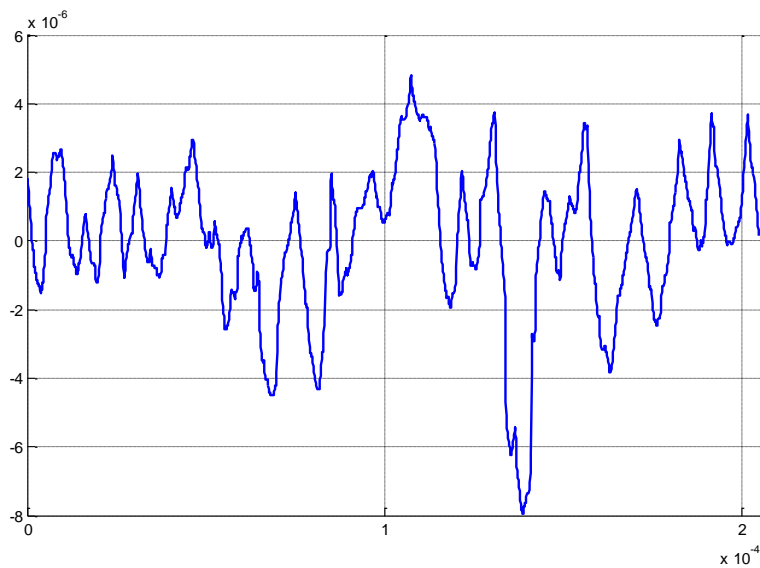6. Remove the linear trend by detrend function in Matlab as Figure 1.10.

Figure 1.10. Roughness profile with the removed linear trend in Matlab file

7. Get   and   from "Sigma" Rule as Figure 1.11.
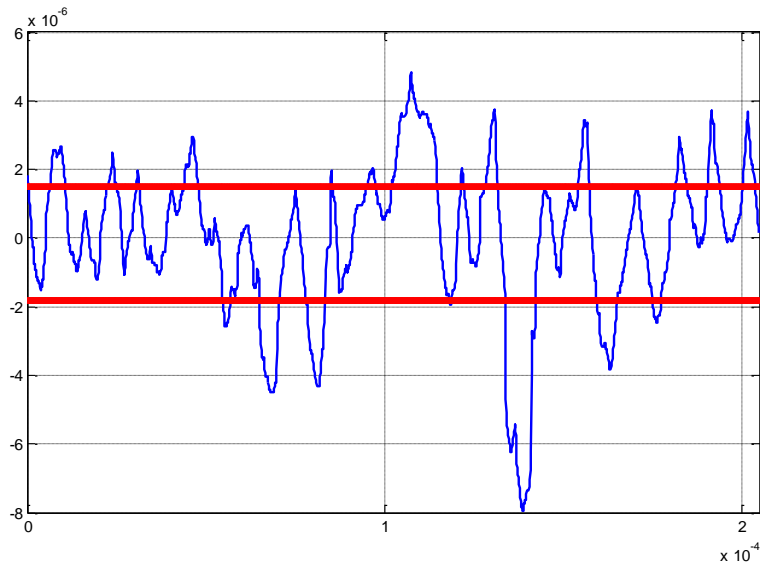
Figure 1.11. Application of "Sigma" rule

1.4 CORRELATION BETWEEN PROFILOMETER DATA AND "SIGMA" RULE

Optical and mechanical profilometers provide data on four main roughness values: Ra, Rq, Rz, and Rt. The definitions of these values are given below.

1. Ra is an arithmetic mean value of the absolute deviations from the mean line on the roughness profile. It is calculated as   , where the sign " " denotes the arithmetic mean value of the roughness profile amplitude.

2. Rq is the r.m.s. value, corresponding to Ra. It is calculated as   .

3. Rz is the mean value of the maximum peak-to-valley height of the profile within the sampling length. It is calculated as   , where   is the average peak value of all maxima within the sampling

length, and   is the average valley value of all minima within the sampling length.

4. Rt is the total height of the profile, which equals to the maximum peak-to-valley height within the assessment (evaluation) length,

.

Optical profilometry gives higher numbers compared to mechanical profilometry. This is due to better resolution of optical profilometers that allow for penetrating into deeper valleys and catching the higher peaks compared to mechanical profilometers. In average, the Rq and Rz data obtained using optical profilometers is twice greater than the corresponding Rq and Rz measured using mechanical profilometers,
and   .

Processing data using "sigma" rule and profilometry allows for suggesting that

$-$ $-$
,   .

This means that, for example, for STD foil, the optical profilometer gives
, the corresponding   μm. Evaluated   μm. The expected values for mechanical profilometer would be   μm, and

.

It is important to mention that profilometers do not directly provide data on average roughness period.

1.5 EVALUATION OF ROUGHNESS

It is difficult if not impossible to evaluate average Λ by just visual inspection, since roughness function is not periodic. It is almost impossible to count, for example, all number of valleys below zero, or all peaks above zero on the sample length, for example, in Figure 1.11, since peak and valley amplitudes are not homogeneous, may consist of a few "subpeaks" or "subvalleys" and not well pronounced and defined.

A new methodology called "Correlation" is used here to extract the Λ. The first three steps are the same with the "Sigma" Rule. The "trace contour" is needed to get from SEM pictures. Then the "trace contour" is shifted to get a new trace. Last, the correlation

factor between old trace and new trace are calculated. When the correlation factor reaches the peak, it is a "Λ". The Λ for the whole trace is the average value of all the "Λ" . The calculation result is shown in Figure 1.12.
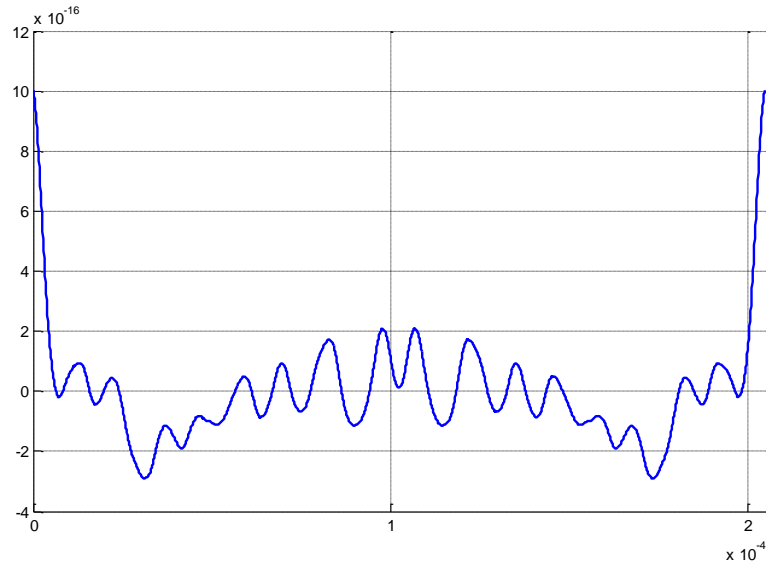
Figure 1.12. Correlation factor vs. shift length

There are 8 peaks, so   .

The sensitivity to the average period value is shown for the Sundstroem-Sanderson model (SSM), when peak-to valley value is taken as   , and there are two different values of Λ= 18.06 μm and 12.24 μm. The curves for conductor loss fifer significantly as shown in Figure 1.13, which would lead to difference in extracting Df value. When roughness Λ is evaluated by "Correlation", the extracted Df is about 18% lower than the result obtained when evaluating roughness using "Sigma" rule, as Figure 1.14 shows.

Figure 1.13. Conductor loss in rough conductor modeled using different Λ

Figure 1.14. Extracted Df data

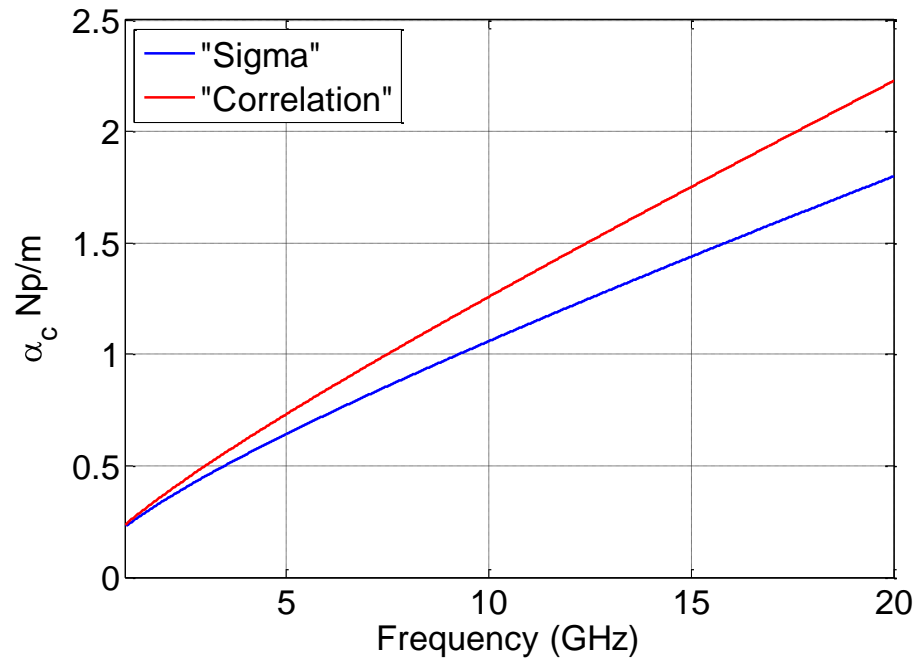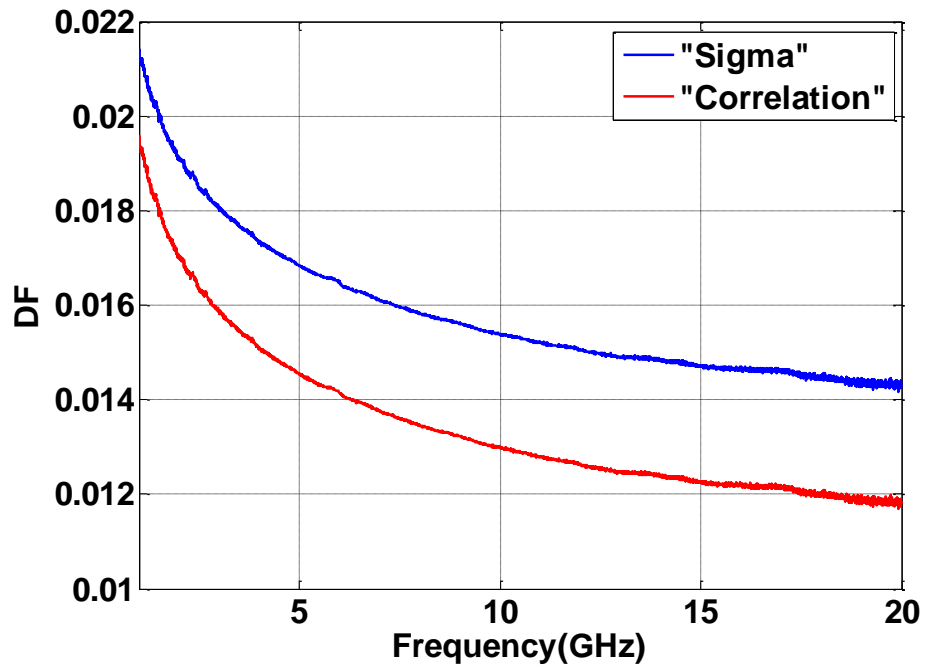Another method named Split Post Dielectric Resonator (SPDR) is used too. SPDR provides an accurate technique for measuring the complex permittivity of dielectric and ferrite substrates and thin films at a single frequency point in the frequency range of 1 to 20 GHz. The SPDR measurement technique is one type of resonance method. Resonators offer the highest available accuracy for measurements of real permittivity, and allow for techniques. A measurement at a discrete frequency point(s) should be adequate, because lossless materials are nearly no dispersive. This means that their dielectric constant and loss tangent will stay constant over a range of frequencies. Figure 1.15 shows the SPDR resonators.

The construction of the SPDR uses new, low loss dielectric materials which make it possible to build resonators having higher Q-factors and better thermal stability than traditional all-metal cavities. The main advantages of the SPDR are:

1. Superior accuracy compared to transmission-reflection methods.
2. Ability to measure low loss materials
3. Convenient, fast and non-destructive measurement of substrates, printed circuit boards, and even thin films.
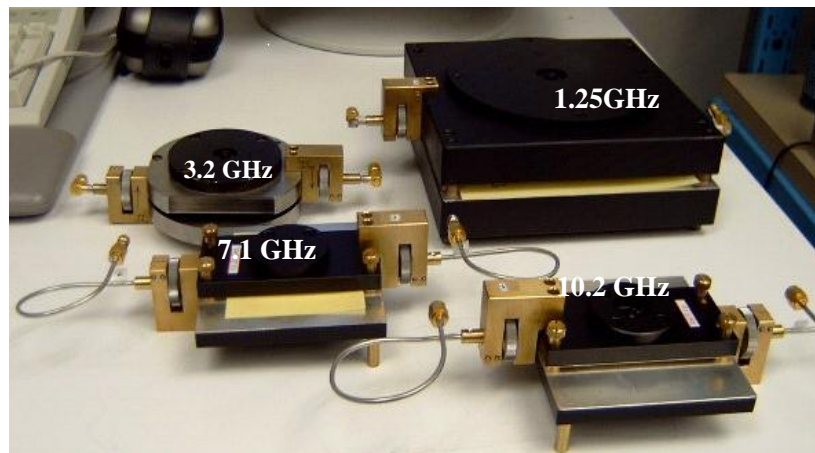

Figure 1.15. SPDR resonators

Table 1.1 shows the measurement result of SPDR, Sigma method and Correlation meshod. From this result, the differnce between SPDR and Sigma method is a little larger than the difference between SPDR and Correlation method. The Corrlation method is more accurcy.

Table 1.1. Comparison of Dk and Df

	Dk			Df		
	SPDR	Sigma	Correlation	SPDR	Sigma	Correlation
1.2 GHz	4.73	4.713	4.713	0.01563	0.02074	0.01883
3.2 GHz	4.67	4.632	4.632	0.01629	0.01789	0.01569
7.1 GHZ	4.64	4.575	4.575	0.01545	0.01607	0.01372
10.2 GHZ	4.56	4.552	4.552	0.01312	0.01535	0.01294

1.6 CONCLUSIONS

In this research, the new "Sigma" rule to evaluate parameters of copper surface roughness in PCB layers is presented. This approach is based on taking SEM images of PCB cross-sections. The approach is automatized by applying image processing tools and Matlab code to evaluate average roughness amplitude and period of roughness function. This information could be used in numerical and analytical modeling, as well as in the DERM method to separate rough conductor loss from dielectric loss.

Data obtained by the proposed "Sigma" rule is correlated to roughness parameters that could be obtained using optical and mechanical profilometers, as well as "manual" approach based on visual evaluating of roughness span on the SEM pictures. Manual approach will give underestimation of Df values on the order of 10% compared to "Sigma" rule.

1.7 REFERENCES

1. E. Bogatin, S. Begley, and M. Resso, "The role of dielectric constant and dissipation factor measurements in multi-gigabit systems," DesignCon, 2007. http://www.designcon.com/newsletter/chapter19.pdf

2. A. Koul, P.K.R. Anmula, M.Y. Koledintseva, J.L. Drewniak, and S. Hinaga "Improved technique for extracting parameters of low-loss dielectrics on printed circuit boards," *Proc. IEEE Symp. Electromag. Compat.,* Aug. 17-21, Austin , TX , 2009, pp. 191-196.

3. A. Rajagopal, B. Achkir, M. Koledintseva, A. Koul, and J. Drewniak, "Material parameter extraction using time-domain TRL (t-TRL) measurements," *Proc. IEEE Symp. Electromag. Compat.,* Aug. 17-21, Austin , TX , 2009, pp. 280-285.

4. A. Deutsch, C. W. Surovic, R. S. Krabbenhoft, and G. V. Kopcsay, "Prediction of losses caused by roughness of metallization in printed circuit boards," IEEE Trans. Adv. Packag., vol. 30, no. 2, 2007, pp. 279–287.

5. V. Khilkevich, M. Koledintseva, V. Sivarajan, D. Liu, B. Achkir, H. Ning, and J. Drewniak, "A systematic approach to PCB material characterization using time domain TRL calibration," DesignCon, 2010, paper 5-TP1, pp. 1-17.

6. S. Hinaga, M. Koledintseva, P. Anmula, and J. Drewniak, "Effect of conductor surface roughness upon measured loss and extracted values of PCB laminate material dissipation factor," Proceedings of the Technical Conference IPC Expo/APEX 2009, Mar.31–Apr.2, 2009, Las Vegas, USA, paper S20-2.

7. M.Y. Koledintseva, A. Koul, P. K.R. Anmula, J.L. Drewniak, S. Hinaga, E. Montgomery, and K.N. Rozanov, "Separating Dielectric and Conductor Loss for Rough Striplines in Printed Circuit Boards," Progress In Electromagnetic Research Symposium (PIERS), Moscow, Russia, Aug. 18-21, 2009, pp. 213-214.

8. S. P. Morgan, Jr., "Effects of surface roughness on eddy current losses at microwave frequencies," J. Appl. Phys., vol. 20, pp. 352–362, Apr. 1949.

9. E.O. Hammerstad and F. Bekkadal, Microstrip Handbook, ELAB report STF44 A74169, the Electronics Research Laboratory, University of Trondheim, Norway, Feb. 1975.

10. S. Groiss, I. Bardi, O. Biro, K. Preis, and K. Richter, "Parameters of lossy cavity resonators calculated by the finite element method," IEEE Trans. Magn, vol. 32, no. 3, pp. 894-897, May 1996.

11. A.E. Sanderson, "Effect of surface roughness on propagation of the TEM mode," in Advances in Microwaves, vol. 7, Academic Press, Cambridge, MA, USA, 1971, pp. 1-57.

12. S. Sundstroem, "Stripline models with conductor surface roughness," Master of Science Thesis, Helsinki University of Technology, Finland, February 2004.

13. H. Braunisch, X. Gu, A. Camacho-Bragado, and L. Tsang, "Off-chip rough-metal-surface propagation loss modeling and correlation with measurements," IEEE Electronic Components and Technology Conf., 2007, pp. 785-791.

14. X. Gu, L. Tsang, and H. Braunisch, "Modeling effects of random rough interface on power absorption between dielectric and conductive medium in 3D problem," IEEE Trans. Microw. Theory Techn., vol. 55, no. 3, pp. 511-517, March 2007.

15. Q.Chen, and N. Wong, "New simulation methodology of 3D surface roughness loss for interconnects modeling," Proc. Design, Automation and Test in Europe (DATE), Apr 2009, pp. 1184-1189.

16. L. Proekt and A. C. Cangellaris, "Investigation of the impact of conductor surface roughness on interconnect frequency-dependent ohmic loss," in Proc. Electron. Compon. Technol. Conf., New Orleans, LA, May 27–30, 2003, pp. 1004–1010.

17. Q. Chen and N. Wong, "An efficient stochastic integral equation method for modeling the influence of conductor surface roughness on interconnect ohmic loss," Proc. Midwest Symp. Circuits and Systems (MWSCAS), Aug 2007, pp. 1417-1420.

18. S. Hall, S. G. Pytel, P. G. Huray, D. Hua, A. Moonshiram, G. A. Brist, and E. Sijercic, "Multigigahertz causal transmission line modeling methodology using a 3-D hemispherical surface roughness approach," IEEE Trans. Microw. Theory Tech., vol. 55, no. 12, pp. 2614–2624, 2007.

19. Y. Shlepnev, A. Neves, T. Dagostino, and S. McMorrow, "Measurement-assisted electromagnetic extraction of interconnect parameters on low-cost FR-4 boards for 6-20 Gb/sec applications," Proc. DesignCon 2009.

20. A. Koul, M.Y. Koledintseva, J.L. Drewniak, and S. Hinaga, "Differential method for separating dielectric and rough conductor loss in printed circuit boards," IEEE Trans. Electromagn. Compat. (submitted on March 19, 2010).

VITA

Fan Zhou was born on April 14th, 1982 in Changsha, China. In June 2004, he obtained his Bachelor's Degree in Hunan University in Electrical Information Engineering, Changsha, China. In April 2007, he obtained his Master's Degree in Beihang University in Electrical Engineering. In August 2008, he enrolled at the Missouri University of Science and Technology to pursue his Master's Degree in Electrical Engineering, during which time he was a graduate research assistant in Electromagnetic Compatibility Laboratory. He received Academic Poster Competition Third Place in IPC APEX EXPO^{TM} 2010. He received his Master's Degree in December 2010.